SANDIA REPORT
SAND2011-6936
Unlimited Release
Printed September 2011

Interfacial Electron and Phonon Scattering Processes in High-Powered Nanoscale Applications

Patrick E. Hopkins

Prepared by
Sandia National Laboratories
Albuquerque, New Mexico 87185 and Livermore, California 94550

Sandia National Laboratories is a multi-program laboratory managed and operated by Sandia Corporation,
a wholly owned subsidiary of Lockheed Martin Corporation, for the U.S. Department of Energy's
National Nuclear Security Administration under contract DE-AC04-94AL85000.

Approved for public release; further dissemination unlimited.

Sandia National Laboratories

Issued by Sandia National Laboratories, operated for the United States Department of Energy by Sandia Corporation.

NOTICE: This report was prepared as an account of work sponsored by an agency of the United States Government. Neither the United States Government, nor any agency thereof, nor any of their employees, nor any of their contractors, subcontractors, or their employees, make any warranty, express or implied, or assume any legal liability or responsibility for the accuracy, completeness, or usefulness of any information, apparatus, product, or process disclosed, or represent that its use would not infringe privately owned rights. Reference herein to any specific commercial product, process, or service by trade name, trademark, manufacturer, or otherwise, does not necessarily constitute or imply its endorsement, recommendation, or favoring by the United States Government, any agency thereof, or any of their contractors or subcontractors. The views and opinions expressed herein do not necessarily state or reflect those of the United States Government, any agency thereof, or any of their contractors.

Printed in the United States of America. This report has been reproduced directly from the best available copy.

Available to DOE and DOE contractors from
U.S. Department of Energy
Office of Scientific and Technical Information
P.O. Box 62
Oak Ridge, TN 37831

Telephone: (865) 576-8401
Facsimile: (865) 576-5728
E-Mail: reports@adonis.osti.gov
Online ordering: http://www.osti.gov/bridge

Available to the public from
U.S. Department of Commerce
National Technical Information Service
5285 Port Royal Rd.
Springfield, VA 22161

Telephone: (800) 553-6847
Facsimile: (703) 605-6900
E-Mail: orders@ntis.fedworld.gov
Online order: http://www.ntis.gov/help/ordermethods.asp?loc=7-4-0#online

SAND2011-6936
Unlimited Release
Printed October 2011

Interfacial Electron and Phonon Scattering Processes in High-Powered Nanoscale Applications

Patrick E. Hopkins
Microscale Sciences and Technologies Department
Engineering Sciences Center
Sandia National Laboratories
P.O. Box 5800
Albuquerque, New Mexico 87185-MS0346

Abstract

The overarching goal of this Truman LDRD project was to explore mechanisms of thermal transport at interfaces of nanomaterials, specifically linking the thermal conductivity and thermal boundary conductance to the structures and geometries of interfaces and boundaries. Deposition, fabrication, and post possessing procedures of nanocomposites and devices can give rise to interatomic mixing around interfaces of materials leading to stresses and imperfections that could affect heat transfer. An understanding of the physics of energy carrier scattering processes and their response to interfacial disorder will elucidate the potentials of applying these novel materials to next-generation high powered nanodevices and energy conversion applications. An additional goal of this project was to use the knowledge gained from linking interfacial structure to thermal transport in order to develop avenues to control, or "tune" the thermal transport in nanosystems.

ACKNOWLEDGMENTS

First and foremost, I would like to express my utmost appreciation to my mentor on this Truman Fellowship project, Leslie Phinney. Leslie went above and beyond her necessary responsibilities as mentor to ensure that my work as a Truman Fellow could excel and exceed my originally planned expectations. Leslie’s help and guidance over the last three years have been unmatchable, and without her selfless efforts and assistance in every aspect of this project, this Truman Fellowship experience clearly would have suffered. I would also like to thank my Department Manager, Dan Rader. The support from Dan, both programmatic and technical, provided the ultimate framework and creative flexibility to truly excel as a Truman Fellow.

As part of this Truman Project, I have had the opportunity to collaborate with several individuals, both internal and external to Sandia. I am greatly appreciative for all of the help and collaborative discussions that I have received from all of my collaborators on this project. Although there is not enough space in this section to thank everybody individually, I would like to express my gratitude to everybody that I’ve interacted with along with way. You all have truly helped to shape this work. Many of these collaborators and colleagues are listed as co-authors on several of the papers resulting from this Truman LDRD; a list of these papers (with co-authors) can be found it the Appendix.

Much of the metal film deposition was performed at the Center for Integrated Nanotechnologies here at Sandia (this work was performed, in part, at the Center for Integrated Nanotechnologies, a U.S. Department of Energy, Office of Basic Energy Sciences user facility). This facility, and its user program, allowed me to fabricate metal transducers for TDTR experiments and structurally characterize many of the samples that I had tested. I am indebted to the various scientists around CINT that have helped me in these tasks.

Finally, I would like to thank the Truman Fellowship Selection Committee for selecting me for this unique, unbelievable opportunity and Yolanda Moreno for all of her assistance during my fellowship. I can’t imagine that scientific life can get much better than that which one experiences as a Truman Fellow. The ability to explore and the intellectual freedom that a Truman Fellow experiences can rarely be found in any other avenue of scientific research. I will truly miss this Truman Fellowship experience.

CONTENTS

1. Introduction 11
2. Background 13
3. Time domain thermoreflectance 15
4. Representative results 21
    4.1. Controlling thermal conductance through quantum dot roughening at interfaces 21
    4.2. Manipulating thermal conductance at metal-graphene contacts via the chemical modification of graphene 28
    4.3. Tunable, ultra-low thermal conductivity of ellipsoidal TiO_2 nanoparticle films 36
    4.4. Minimum thermal conductivity considerations in aerogel thin films 42
5. Conclusions 49
6. References 51
Appendix: List of published papers from LDRD 61
Distribution 66

FIGURES

Figure 1. Thermal boundary conductances at various solid interfaces. Typical values span over two orders of magnitude. For comparison, the equivalent conductance of various thicknesses of SiO_2 are shown as the solid lines....................13

Figure 2. (a) Thermal boundary conductance across Al/Si interfaces in which the Si was chemically roughened prior to Al film evaporation, leading to rough Al/Si interfaces. The RMS roughness was characterized with AFM analysis. (b) Thermal boundary conductance across Al/sapphire interfaces in which the sapphire was subjected to varying degrees of proton implantation. At the maximum irradiation dose, h_K decreases by over an order of magnitude. The key here is that the proton doses, and therefore degree of substrate damage, is completely controllable. 14

Figure 3. Schematic of TDTR experiment built at Sandia as part of this LDRD. 18

Figure 4. Thermal sensitivities in TDTR to h_K and κ of the substrate in 100 nm Al/Si and Al/SiO_2 systems. 19

Figure 5. TDTR data from a 117 nm Al film evaporated on a Si substrate along with the best fit from the thermal model. The thermophysical properties determined from the model best fits are G = 210 MW m^{-2} K^{-1} for the Al/Si interface and κ = 141 W m^{-1} K^{-1} for the Si substrate. 20

Figure 6. Atomic force microscrope images and representative line scans of the QD roughened surfaces studied in this work. These specific surfaces have RMS roughnesses of (a) 0.28 nm from Ge QDs, (b) 0.53 nm from Ge QDs, (c) 1.38 nm from Ge QDs, (d) 2.16 nm from GeSi QDs, and (e) 4.46 nm from GeSi QDs. The representative line scans of each AFM are shown in (f)....................22

Figure 7. Measured thermal conductance of the six Al/Si interfaces fabricated in this work as a function of temperature. The QD patterning on the surface of the Si causes reduction in h_K. In addition, the measured h_K on the six samples converges at low temperature indicating that phonons are not as readily affected by the roughness at low temperatures, indicative of longer-wavelength phonon-dominated transport. Also shown in this figure are calculations of the DMM. Including the thermal resistance associated with the native oxide layer on the surface of the Si greatly improves the agreement between the DMM and the Al/Si interface with no QD patterning. The roughness is accounted for by assuming that short wavelength phonons are more readily scattered at rough interfaces that have greater coverage of QDs, as described by Eq. (25). We plot the DMM using the phonon attenuation parameter given in Eq. (25) as the dashed lines assuming an QD RMS roughness of δ = 0.5 nm or 5.0 nm. Our model that accounts for additional scattering by the QD's agree well in both value and trend as the corresponding data with similar RMS roughnesses. 23

Figure 8. Thermal conductance as a function of RMS roughness across the series of structurally variant Al/Si interfaces at 300 K. Calculations of Eq. (24) at T = 300 K as a function of δ are also shown. We find that β = 0.0040 leads to a good agreement between the model and experimental data. 26

Figure 9. (a) High resolution C1s spectra of untreated graphene and plasma treated graphene. The inset shows the oxygen treated sample along with peak fitting results. (b) Averaged Raman spectra for each of the films analyzed in this study. While the reference film shows a high level of crystallinity, functionalization induces nanocrystallinity in the H-treated film, and begins to induce amorphous regions of sp^3 carbon in the oxygen treated film. 29

Figure 10. Measured thermal boundary conductances on the Al/SLG/SiO_2 sample (filled squares), the hydrogen functionalized sample (filled circles), and the oxygen functionalized sample (filled diamonds). The hydrogen functionalization process, which introduces disorder on the SLG, also leaves the SLG surface chemically inert and does not leave any additional bonding mechanism for the Al to the SLG. The slight decrease in h_K that we observe due to hydrogen functionalization is therefore due to the disorder at the Al/SLG interface. Functionalizing the SLG with oxygen leaves the graphene surface reactive leading to increased covalent bonds linking the Al to the SLG, which results in a higher phonon transmission and increase in h_K. For comparison, we also show h_K across SLG/SiO_2 (open circles – Ref. 16) and Al/graphite (open squares – Ref. 94) interfaces. Using these two measured conductances with Eq. (1), we can predict the Al/SLG/SiO_2 interface assuming that the Al/graphite h_K is similar to Al/SLG and that the Al/SLG and SLG/SiO_2 conductances can be separated. The resulting conductance, which is depicted by the solid line, is in very good agreement with our Al/SLG/SiO_2 measurements, indicating that the Al/SLG/SiO_2 thermal boundary conductance can be described by two separate conductances – Al/SLG and SLG/SiO_2. 31

Figure 11. Thermal boundary conductance across our Al/SLG (filled squares) and Al/O-SLG (filled diamonds) interfaces derived from our experimental measurements across the Al/SLG/SiO_2 and Al/O-SLG/SiO_2 interface along with Eq. (27) and the data from the SLG/SiO_2 interfaces.[16] The thermal transport across the Al/SLG interface increases by a factor of two with oxygen functionalization of the graphene. Our derived values for h_K across the Al/SLG interface are in good agreement with conductances measured across Al/graphite (open squares – Ref. 94) and Al/diamond interfaces (open circles – Ref. 105). Similarly, our derived values for Al/O-SLG h_K is in good agreement with Al/O-diamond measurements (filled circles – Ref. 106). We model the thermal conductance across the Al/SLG interface with the DMM, as shown by the solid line. We adjust the velocity of the SLG in our DMM calculations to model the Al/O-SLG thermal boundary conductance (dashed line), and find that the resultant velocity in the oxygenated SLG is about a factor of two higher than the non-functionalized sample. This is indicative of the increase in covalent bonds between the Al and the SLG via the oxygen adsorbates. 33

Figure 12. Ratio of thermal boundary conductance Al/O-SLG to Al/SLG (filled squares). For comparison, we also plot the ratio of h_K across the Al/O-diamond interface[106] to the Al/diamond interface[105] (filled circles). These ratios are very similar, especially at elevated temperatures, which would be indicative of a similar increase in the elastic constants at the Al-O bond compared to the Al-graphene or Al-diamond bond. We plot the ratio of h_K across a Au/(2nm)Ti/SLG/SiO_2 interface[5] to h_K across an Au/graphite interface[94] (filled triangles). The two conductances are nearly identical over the entire temperature range (i.e., Au/(2nm)Ti/SLG:Au/graphite ~ 1). Where the Ti will increase the bond strength, Au is a very soft material with low phonon velocities and weak elastic constants. Therefore, the phonon flux in gold is so low that regardless of the strength of the bond at the Au/SLG or graphite interfaces, the phonon transmissivity will always be limited by the phonon flux in the Au..........................35

Figure 13. SEM images of the deposited films. (a) $\phi = 0.24$, $v = 125$ μm/s, P_2 = 0.335 (b) $\phi = 0.24$, $v = 1500$ μm/s, P_2 = 0.185 (c) $\phi = 0.52$, $v = 125$ μm/s, P_2 = 0.730 (d) $\phi = 0.52$, $v = 1500$ μm/s, P_2 = 0.885. The arrow denotes the coating direction. The scalebar is 1 μm.. 37

Figure 14. The thermal conductivity of the films (k) measured at the room temperature as a function of order parameter (P_2), estimated from SEM images as described in the supporting information. The minimum thermal conductivity of TiO2 is also shown ($\kappa_{\min}$ – Eq. (31)). The orientational ordering, which is controllable during the assembly process, can be use to tune the thermal conductivity across the theoretical minimum limit. 38

Figure 15. Thermal conductivities of three different films – an ordered film (2b), a disordered film (1d), and a moderately ordered/disordered film (2d). Representative error bars are shown which represent the standard deviation calculated from the 5 different measurements on each sample. For comparison, we also plot the thermal conductivity of bulk, single crystalline TiO_2 (Ref. 124), a polycrystalline sputtered film with ~17 nm grain size,[125] and an amorphous TiO_2 film.[126] The thermal conductivity of the nanoparticle based films nearly an order of magnitude lower than the sputtered TiO_2 film with similar grain sizes. The measured thermal conductivities of the nanoparticle films have similar values of κ as the amorphous film but temperature trends similar to the polycrystalline sputtered film indicating that the phonon transport in the nanoparticle films is not limited by the interatomic spacing or lack of periodicity as in the amorphous film. This implies that three-phonon scattering and boundary scattering are still dominant phonon scattering events in these nanoparticle films with extremely low thermal conductivity...39

Figure 16. Thermal conductivity of film 2b (ordered) and film 1d (disordered) as a function of temperature. The temperature trends of the experimental data are different than those predicted by the minimum limit. We model the thermal conductivity of the films by considering Umklapp, impurity and grain boundary scattering and interparticle thermal boundary resistance. d = 260 nm and d = 48 nm correspond to the length and width of a TiO_2 nanoparticle, respectively, and are the bounds on the distance a phonon can propagate before scattering. 42

Figure 17. Scanning electron microsocpy image of the (a) cross section and (b) top view of a thin film aerogel. The scale bars are 500 nm. 43

Figure 18. TDTR data from the EISA and aerogel films along with data from the sample with no film (i.e., air). The solid lines represent the predictions from the thermal model for various reductions in the SiO_2 sample thermal conductivity. 44

Figure 19. Thermal conductivity as a function of volumetric atomic number density of silicon and oxygen for the EISA, aerogel, and calcined-aerogel films along with bulk SiO_2,[49] a sputtered

SiO_2 thin film,[13] and bulk SiO_2 aerogels.[139,145] Predictions from the theoretical “porous minimum limit” to the thermal conductivity of SiO_2 (solid line - Eq. (35)) that is derived in this work shows good agreement with the thermal conductivity of the porous silica structures..................46

Figure 20. Thermal conductivity cover glass substrate and the two aerogel films from this work as a function of temperature. We plot our ``porous minimum limit" that is given in Eq. (35). Our “porous minimum limit” agrees well with our measured κ on the aerogel films well. We also show the measured thermal conductivity of our cover glass (VWR Cover Glass #48368040) with previously measured values of Corning Pyrex #7740 and bulk SiO_2 for comparison.[20,49] ...47

NOMENCLATURE

A	Power absorbed at the sample surface (W)
C	Heat capacity (J m^{-3} K^{-1})
D	Thermal diffusivity (m^{2} s^{-1})
d	Film thickness or characteristic length (m)
f	Modulation frequency (Hz)
K	Transform variable (m^{-1})
H	Solid-fluid volumetric heat transfer coefficient (W m^{-3} K^{-1})
h_{K}	Thermal boundary conductance, or Kaptiza conductance (W m^{-2} K^{-1})
$\hbar$	Planck's constant divided by 2π (J s)
n	Bose-Einstein distribution function
n_{bulk}	Bulk atomic density (m^{-3})
n_{p}	Porous material atomic density (m^{-3})
P	Volumetric absorbed power (W m^{-3})
q	Phonon flux (J m^{-2})
q_T	Thermal wavevector (m^{-1})
R_{K}	Thermal boundary resistance, or Kapitza resistance (W^{-1} m^{2} K)
r	Radial coordinate (m)
T	Temperature (K)
t	Time (s)
v	Phonon velocity (m s^{-1})
w	1/e^{2} laser spot radius (m)
X	Real component of lock-in frequency response
Y	Imaginary component of lock-in frequency response
Z	Lock-in transfer function
z	Direction normal to the sample surface (m)

Greek symbols

β	Phonon attenuation constant
γ	Interfacial roughness parameter
κ	Thermal conductivity (W m^{-1} K^{-1})
λ	Phonon wavelength (m)
χ	Proportionality constant in lock-in transfer function
θ	Temperature rise (K)
Φ	Porosity
ϕ	Phase of lock-in signal
ω	Angular frequency (rad s^{-1})
τ	Pump-probe delay time (s)
τ_j	Phonon scattering time of polarization j (s)
ζ	Phonon interfacial transmission coefficient

1. INTRODUCTION

Thermal management has assumed a critical role in the design and development of electronic devices, power generation modules, and waste energy harvesting techniques. In these applications, performance depends vitally on the thermal conductivity (κ) of the component materials. Yet, while the electrical conductivity in a typical semiconductor system can be tuned across 10 orders of magnitude via doping, no such analog, in terms of absolute control and precision, exists with κ, regardless of mechanism or material system.[1] However, thermal transport processes on the nanoscale present such a regime in which exciting and unique processes such as boundary scattering, ballistic transport, and wave-effects offer potential new degrees of freedom in the thermal engineering of material systems.[2,3]

The ability to precisely control the heat transfer in nanostructures would provide novel thermal solutions for a wide variety of applications. For example, power dissipation limits the performances of electronic systems from individual microprocessors to data centers. In silicon-based microprocessors (by far the most commonly implemented technology), operation beyond a few GHz is not possible due to on-chip power densities exceeding 100 W/cm^2 – higher than a typical hotplate[4] and far greater than typical cooling capabilities. Alternatively, controlled reduction in thermal transport can be very beneficial in applications involving thermal storage, thermal generation, or thermoelectric cooling. For example, in nano-thermoelectric composites, reducing the thermal transport in the nanomaterials can lead to a reduction in the overall thermal conductivity of the thermoelectric module. Given that the efficiency of the thermoelectric device is inversely related to the thermal conductivity of the materials in the device, the ability to control the reduction in κ can lead to a controlled increase in the device efficiency (i.e., the Figure of Merit, ZT).[5] Clearly, the ability to control the thermal properties of materials would benefit several applications.

This desired thermal tunability of nanomaterials, however, is not a trivial task. This is mainly due to the fact that as length scales of nanomaterials approach thermal carrier mean free paths and wavelengths, the thermal transport in nanosystems becomes primarily driven by the conduction of energy across material interfaces, characterized by the thermal boundary conductance. Interfacial thermal transport in nanosystems has been a very active area of research over the past decade.[3,4] However, there are still many aspects of this field that area poorly understood, making this thermal tunability a "pipe dream" until recently. Pernot *et al.*[6] demonstrated precise control of thermal conductivity in Si/Ge nanodot superlattice structures by varying the period spacing. Their structures were relatively small (15 nm total thickness) and contained upwards of 10 nanodot layers, making the interpretation of the origin of the thermal conductivity control relatively difficult due to substrate and other interface effects. However, the controllable, and low thermal conductivity of the samples reported in Pernot *et al.*'s [6] work is very encouraging, and can give an avenue for thermal control with structures of bigger feature sizes to utilize this control on a larger, scalable device. The key to this goal, however, is to fully understand the origin of this thermal control, which lies in the physics of phonon transport at a structurally variant interface.

The overarching goal of this Truman LDRD project was to explore mechanisms of thermal transport at interfaces of nanomaterials, specifically linking the thermal conductivity and thermal boundary conductance to the structures and geometries of interfaces and boundaries. Deposition, fabrication, and post possessing procedures of nanocomposites and devices can give rise to interatomic mixing around interfaces of materials leading to stresses and imperfections that could affect heat transfer. An understanding of the physics of energy carrier scattering processes and their response to interfacial disorder will elucidate the potentials of applying these novel materials to next-generation high powered nanodevices and energy conversion applications. An additional goal of this project was to use the knowledge gained from linking interfacial structure to thermal transport in order to develop avenues to control, or “tune” the thermal transport in nanosystems.

This LDRD has resulted in 39 refereed journal publications, with an additional 2 publications currently under review and 1 invited book chapter. This SAND report will only discuss a few of these publications in depth (1 published and the 3 publications currently under review). A full list of all the journal publications is given in the Appendix. In the next section, the concept of thermal boundary conductance, which is the major resistance of heat in nanosystems, is discussed. Some of the PI’s works exhibiting the influence of interfacial structure on thermal boundary conductance are highlighted. In Section 3, the experimental system built by the PI (Time Domain Thermoreflectance – TDTR) is detailed, and the thermal analysis is outlined and example data fits are shown. Section 4 goes on to discuss 4 different experimental studies examining thermal transport in nanosystems, which exemplifies the effects of boundaries and interfaces, along with the ability to control thermal transport with nanoscale structures. Finally this LDRD project is summarized in Section 5.

2. BACKGROUND

The thermal transport across solid interfaces is quantified by the thermal boundary conductance, h_K, which is the proportionality constant that relates the heat flux across an interface to the temperature drop associated with the interfacial region, i.e., $h_{\mathrm{K}} = q_{\mathrm{int}} / \Delta T$. The thermal boundary conductance across solid interfaces can be driven by various particle scattering processes, such as electron-electron scattering,[7,8] electron-phonon scattering,[9-11] or phonon-phonon scattering.[12] For these various scattering processes, the transmission of carrier energy across the interface is related to the density of carriers in the two adjacent materials comprising the interface; for example, the well known Diffuse Mismatch Model (DMM),[12] which describes phonon transport across interfaces, theorizes that interfacial phonon transmission is driven by the differences in the phonon density of states between the two material comprising the interface. Figure 1 shows the thermal boundary conductance as a function of temperature for various interfaces in which h_{K} is dominated by phonon scattering.[13-19] Along with these data, the equivalent conductances of various thicknesses of SiO_2 are indicated by the solid lines; this equivalent conductance is calculated by $h_{\mathrm{SiO2}} = \kappa_{\mathrm{SiO2}} / d$ where κ_{SiO2} is the thermal conductivity of SiO_2 and d is the thickness, as indicated in the figure.[20] Typical values for thermal boundary conductance at solid interfaces span about 2.5 orders of magnitude, depending on the materials comprising the interfaces. Most of these values correspond to an equivalent conductance of 10 – 100 nm of SiO_2.

A tremendous amount of work has focused on measurements and theory on thermal transmission across solid interfaces assuming a perfectly abrupt or ``flat" junction between two materials (see Ref. 3 and 4 for extensive reviews). However, measurements of thermal transport across non-ideal interfaces have been much less frequently studied.

The PI has extensively investigated the effects of random roughness and disorder on h_K; he measured h_K across a series of Cr/Si interfaces with varying degrees of elemental mixing around the solid interface finding that phonon-phonon scattering in a so-called mixing region of Cr and Si caused a decrease in h_{K}.[21] The PI also found that RMS roughness at Si surfaces causes variations in h_K across Al/Si interfaces.[22] Figure 2a shows the measured thermal boundary conductance across Al/Si interfaces as a function of RMS roughness, δ, of the Si surfaces. The Si wafers were chemically etched prior to Al film evaporation. The chemical etching procedure caused random roughening on the Si surface which created a variety of rough Al/Si interfaces. The RMS roughnesses of these Si surfaces were determined from atomic force microscopy (AFM) analysis prior to Al film

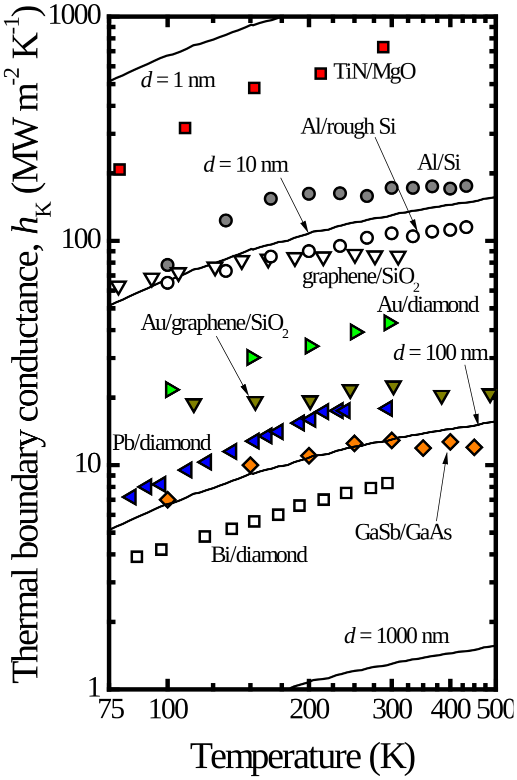

Fig. 1. Thermal boundary conductances at various solid interfaces. Typical values span over two orders of magnitude. For comparison, the equivalent conductance of various thicknesses of SiO_2 are shown as the solid lines.

deposition. There is a clear dependency in the measured h_K on the RMS roughness. This dependency on RMS roughness is not predicted by the DMM (dashed line). However, a model based on the DMM that accounts for additional phonon scattering events around the Al/Si interface (such as phonon-impurity scattering) captures the measured data well. This model is shown as the solid line in Fig. 2a. This indicates that nanometer changes in surface roughness can lead to changes in the thermal transport across interfaces.

In another study, the PI investigated the effects of ion bombardment on the thermal boundary conductance across metal/semiconductor interfaces.[23] The substrates were irradiated with protons which damage the crystalline lattice, causing significant damage and some degree of amorphization. The measured thermal boundary conductances across Al/sapphire interfaces subjected to controlled doses of protons are shown in Fig. 2b. With increased proton dose, the thermal boundary conductance exhibits a continued reduction. At the highest proton dose, the Al/sapphire h_K decreases by over an order of magnitude. This indicates that damage and change in periodicity of the crystalline lattice can lead to a reduction in thermal boundary conductance.

These experimental results have been accompanied by various theories by the PI that have elucidated the major mechanisms affecting phonon scattering around rough interfaces.[21,23-25] The roughness and change in structure around solid interfaces gives rise to phonon-static impurity scattering events which leads to the reduction in thermal boundary conductance. The key is to be able to control these phonon scattering events. Clearly, precise control of these mechanisms, which ties into controlling the interface structure, would give an avenue to control phonon scattering and the subsequently control h_K.

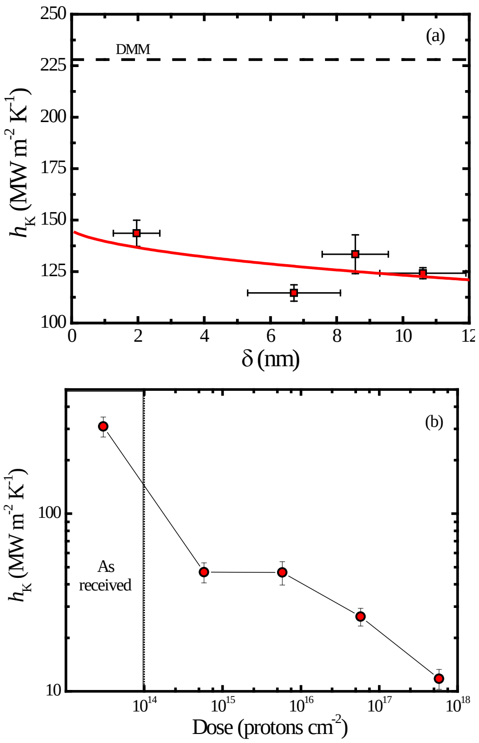

Fig. 2. (a) Thermal boundary conductance across Al/Si interfaces in which the Si was chemically roughened prior to Al film evaporation, leading to rough Al/Si interfaces. The RMS roughness, *δ*, was characterized with AFM analysis. (b) Thermal boundary conductance across Al/sapphire interfaces in which the sapphire was subjected to varying degrees of proton implantation. At the maximum irradiation dose, h_K decreases by over an order of magnitude. The key here is that the proton doses, and therefore degree of substrate damage, is completely controllable.

3. TIME DOMAIN THERMOREFLECTANCE

Pump-probe transient thermoreflectance techniques utilizing short pulsed lasers have been extensively used to measure thermal conductivity, κ, and thermal boundary conductance, h_K, of nanomaterials and interfaces of nanomaterials, such as κ in metal films,[26] dielectric films,[27] phase change materials,[28] thermally anisotropic materials,[29] superlattice structures,[30] and layered nanolaminates,[31,32] and h_K across metal-metal,[7] metal-dielectric,[14,17,21,33,34] and metal-liquid[35] interfaces. These transient thermoreflectance techniques measure the change in reflectance of the surface of a material as a function of time after a short pulsed heating event. The change in reflectance is related to the temperature change of the electrons in the material, and the measured change in temperature as a function of time is then related to κ and h_K through a conduction heat equation.

The experiments and analyses in this LDRD are focused on pulsed laser heating from a Ti:Sapphire oscillator with a fundamental output of 90 fs pulses at 80 MHz (12.5 ns between laser pulses); the laser pulses are then further modulated at with an electro-optic modulator to create a modulated heating event at the sample surface, and the temperature decay on the surface of the samples from this modulated heating events are monitored over ~4 - 8 ns. This experiment is referred to as Time Domain Thermoreflectance (TDTR). The laser pulses are treated as delta functions in time due to the ultrashort pulse width compared to the time delay of the experiments. The thermal penetration depth of the modulated heat source is estimated by $\sqrt{D/(\pi f)}$, where D is the diffusivity and f is the modulation frequency. For most solids subjected to MHz thermal modulation rates, the thermal penetration depth is anywhere from 100 nm – 10 μm. To ensure mostly cross plane (one dimensional) transport, the laser spot size of the modulated heating source should be greater than the thermal penetration depth. Typical TDTR experiments utilize pump spot sizes on the order of 10 μm. Therefore, for low diffusivity systems, the thermal transport measured in TTR experiments is nearly entirely cross plane due to the small thermal penetration depth.

In typical TDTR experiments, the pump and probe beams have spatially Gaussian intensity distributions when incident on the film surface. Therefore, depending on the relative sizes and overlap of the beams, the radial distributions of the pump beam could affect the temperature measured by the probe beam. In this case, the assumption a one dimensional heat transfer model may not be applicable since it assumes that the probe reflectance, or the measured change in temperature, is measuring a uniformly heated plane at the surface of the film. To correct for this, Cahill[36] derived an expression for $\theta(r)$, the temperature rise at the surface of the film, assuming radial spreading in a half-sphere from the pump pulse. This begins by considering the axially symmetric heat equation in cylindrical coordinates is given by

$$C_1 \frac{\partial \theta_1(r,z,t)}{\partial t} = \kappa_{1,z} \frac{\partial^2 \theta_1(r,z,t)}{\partial z^2} + \frac{\kappa_{1,r}}{r} \frac{\partial}{\partial r}\left(r \frac{\partial \theta_1(r,z,t)}{\partial r} \right), \tag{1}$$

where r is the radial coordinate, the subscript r and z denote the radial and cross plane conductivities, and C is the volumetric heat capacity. Taking the Hankel transform along the radial, planar dimension, then applying a Fourier transform, Eq. (1) leads to

$$\frac{\partial^2 \theta_1(r,z,\omega)}{\partial z^2} = q_{T,1}^2 \theta_1(r,z,\omega), \tag{2}$$

where ω is the angular frequency of the pump pulses and

$$q_T^2 = \frac{\kappa_r K^2 + iC\omega}{\kappa_z}, \tag{3}$$

where K is the transform variable. This anisotropic q was used by Schmidt *et al.*[29] to determine the directionally dependent thermal conductivities of graphite in anisotropic structures. In this work, however, we consider isotropic materials and we are only interested in cross plane properties, so $q_T^2 = K^2 + (iC\omega/\kappa)$.

The temperature change on the surface of the film due to heat flow through underlying materials is easily taken into account through Carslaw and Jaeger's solution for steady periodic temperature change in composite slabs.[37] A convenient implementation of this is presented by Feldman[38] and discussed here. The change in surface temperature of material 1 is given by

$$F(k) = \frac{1}{\gamma_1}\left(\frac{F_{T1}^+ + F_{T1}^-}{F_{T1}^- - F_{T1}^+}\right), \tag{4}$$

where F_{T1}^+ and F_{T1}^- are temperature change coefficients related to the forward and backward propagating waves on the surface (top side) of material 1 and where $\gamma = \kappa q_T$. The forward and backward propagating wave at the top side of material 1 are related to the waves on the bottom side through

$$\begin{bmatrix} F_{T1}^+ \\ F_{T1}^- \end{bmatrix} = \begin{bmatrix} \exp[-q_1 d_1] & 0 \\ 0 & \exp[q_1 d_1] \end{bmatrix} \begin{bmatrix} F_{B1}^+ \\ F_{B1}^- \end{bmatrix}, \tag{5}$$

where d is the material thickness. For material 1, the top side is assumed at the slab/air interface and the bottom side is assumed as the interface between material 1 and material 2 (i.e., film/substrate). Given a thermal boundary conductance, h_{K}, between material 1 and material 2, the temperature at the top of slab 2 is related to the temperature at the bottom side of slab 1 by

$$\begin{bmatrix} F_{B1}^+ \\ F_{B1}^- \end{bmatrix} = \frac{1}{2} \begin{bmatrix} 1 + \frac{\gamma_2}{\gamma_1} - \frac{\gamma_2}{h_{\mathrm{K},12}} & 1 - \frac{\gamma_2}{\gamma_1} + \frac{\gamma_2}{h_{\mathrm{K},12}} \\ 1 - \frac{\gamma_2}{\gamma_1} - \frac{\gamma_2}{h_{\mathrm{K},12}} & 1 + \frac{\gamma_2}{\gamma_1} + \frac{\gamma_2}{h_{\mathrm{K},12}} \end{bmatrix} \begin{bmatrix} F_{T2}^+ \\ F_{T2}^- \end{bmatrix}. \tag{6}$$

Assuming a bulk substrate, heat cannot reach the bottom side of slab 2 at rates comparable to the modulation frequency (semi-infinite), so there is no thermal buildup of waves and

$$\begin{bmatrix} F_{T2}^+ \\ F_{T2}^- \end{bmatrix} = \begin{bmatrix} 0 \\ \exp[-q_2 d_2] \end{bmatrix}. \tag{7}$$

With Eqs. (4) – (6), this approach gives a straight forward method to solve for heat conduction through several materials and interfaces via successive implementation of Eqs. (5) and (6) for each layer and then Eq. (7) for the final, semi-infinite layer. This is much less computationally expensive than solving the heat equation in the time domain for each interface and material.

To determine the temperature oscillations on the surface of material 1 with the frequency domain model in Eq. (2) due to cooling from underlying layers described by Eqs. (5) – (7), a top surface boundary condition must be imposed. In TDTR, this is described by first convoluting Eq. (4) with the pump-beam distribution,[29] given by

$$\theta(k) = F(k)\frac{A}{2\pi}\exp\left[\frac{-k^2 w_{PU}^2}{8}\right], \tag{8}$$

where w_{PU} is the 1/e^2 radius of the pump beam, and then taking the weighted average of the surface temperature oscillations by the probe beam of 1/e^2 radius w_{PR} to yield[36]

$$\theta(r,0,\omega)=\frac{A}{2\pi}\int_0^\infty F(k)\exp\left[\frac{-k^2\left(w_{PU}^2+w_{PR}^2\right)}{8}\right]kdk\,. \tag{9}$$

Equation (9) gives the change in temperature as a function of heating event modulation frequency at the surface of the film. This axially symmetric thermal model has been used by several groups to determine h_K[13,17] and, due to its simple extension to multilayer structures, thermal conductivity of thin layers and multilayered structures.[27,31,32,39-41] Note, that in this development, the pump source is assumed to be applied only at the surface, so substrate effects on the pump distribution are nonexistent. Although Eq. (9) accounts for radial effects in TDTR, it does not give the response as a function of time, which is measured in TDTR. To examine the temporal evolution of Eq. (9), the response of the material systems to the laser and modulation repetition rates must be considered. This is described in detail through lock-in response functions.

Due to the relatively small change in voltage due to the probe thermoreflectance response as compared to the DC voltage from the reflected probe, a lock-in amplifier is used in TDTR data collection to monitor the temporal decay in the thermoreflectance response occurring at the modulation frequency of the heating event. The output of the lock-in amplifier serves to relate frequency domain models to the time domain. The lock-in output will be the magnitude, R, and phase, ϕ, of the probe signal at the heating event modulation frequency. Mathematically, the lock-in output takes the form of[29]

$$R\exp[i(\omega_0 t+\phi)]=Z(\omega_0)\exp[i\omega_0 t], \tag{10}$$

where ω_0 is the modulation frequency of the pump pulses and $Z(\omega_0)$ is the transfer function of the lock-in. In the frequency domain, the transfer function can be represented as[36]

$$Z(\omega_0)=\frac{(2\pi)^2\chi}{\omega_s^2}\sum_{M=-\infty}^{\infty}\theta(\omega_0+M\omega_s)\exp[iM\omega_s\tau], \tag{11}$$

where θ is calculated with Eq. (9), ω_s is the modulation frequency of the laser system (not the modulation frequency of the heating event; so for a Ti:Al$_2$O$_3$ oscillator, $\omega_s/2\pi$ is approximately 80 MHz), τ is the delay time between the pump and probe pulses, χ is a constant that is related to the gain of the electronics, the power of the pump and probe pulses, and the thermoreflectance coefficient of the material. The thermoreflectance coefficient, which relates the change in temperature from the model to the change in reflectance measured in the experiment, is a material property that is related to the band structure, electronic transitions, and dielectric function.[42] In the low perturbation regime (i.e., small temperature rise of the film compared to ambient) in which this work is focused, the change in reflectance is linearly related to the change in temperature and the thermoreflectance coefficient is a constant. From Eq. (11), the lock-in outputs are given by

$$X=\mathrm{Re}[Z(\omega_0)], Y=\mathrm{Im}[Z(\omega_0)], \tag{12}$$

where X and Y are the real and imaginary components of the measured frequency response, and

$$R=\sqrt{X^2+Y^2}, \phi=\tan^{-1}\left[\frac{Y}{X}\right]. \tag{13}$$

By nature of Eq. (11), pulse-to-pulse heating and thermal accumulation due to pump modulation is taken into account with a frequency domain model (note that, in this work, when calculating temporal response with the frequency domain models, it is implied that the frequency domain models are used in conjunction with Eq. (11) to determine the time domain response). Although a similar model can be derived for pulse accumulation in the time-domain,[29] it has not been used in previous works, most likely due to the numerical cost which negates the benefit of using the simplified model in the time domain. Even with exact analytical forms of the conduction thermal diffusion equation obtained by Laplace transforms,[43] accounting for pulse accumulation can be computationally expensive compared to that in the frequency domain since, in the time domain, the solution must take into account the multiple pulses in the pump modulation envelope occurring every 12.5 ns while providing picosecond resolution in the analysis.

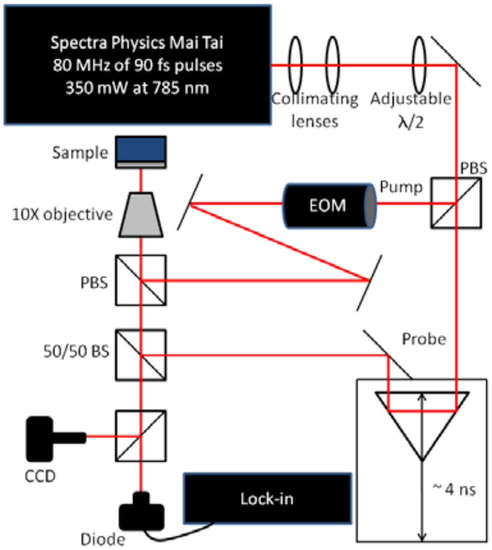

Fig. 3. Schematic of TDTR experiment built at Sandia as part of this LDRD.

The thermal model and lock-in transfer function discussed above are applied to data determining h_K and κ from pump-probe measurements using the TDTR experimental setup at Sandia National Labs. The experimental setup, shown in Fig. 3, is nearly identical to similar setups that exploit coaxial pump-probe geometries discussed in previous works.[3,29,44] The laser pulses in this specific experimental setup emanate from a Spectra Physics Mai Tai oscillator outputting 350 mW of power at a repetition rate of 80 MHz and pulse widths of 90 fs at a wavelength of 785 nm. The setup shown in Fig. 3 differs from previous collinear setups by two slight modifications. First, the pulses are first passed through a pair of collimating lenses to minimize probe divergence at the sample surface due to the variable delay stage; upon characterization with a sweeping knife edge,[45] the probe (and pump) radius at minimum pump-probe delay is ~ 15 μm and exhibits less than 1 μm divergence at maximum delay. Then, the pulse train passes through an adjustable half-waveplate before being split into the pump and probe paths by a polarizing beam splitter cube (PBS); this fixes the pump and probe path as orthogonally polarized and the waveplate therefore allows for easy adjustment of the pump and probe powers; the relative pump and probe powers are adjusted to achieve a maximum thermoreflectance signal. We vary the temperature of the sample of interest by mounting the sample in a cryostat with optical access that can operate from 77 – 500 K.

The data must be post processed to remove any electronic noise that would lead to unwanted signals. These signals would appear as a change in the imaginary component of the signal, Y, as τ crosses zero, since Y should not change as the pump-probe delay time goes from negative to positive. Schmidt *et al.* [29] determined the change in the real and imaginary components of the signals and calculated a phase noise to subtract from the data. Cahill[36] corrected for this by multiplying the signal by a small phase factor. Here, we employ the following correction: the change in the lock-in signals as the delay time crosses $\tau = 0$, ΔX and ΔY, are computed from the collected data. The measured signals are corrected by rotating the signal in the complex plane, so that the corrected values for X and Y are given by[46]

$$X_c = X\cos\left[\tan^{-1}\left[\frac{\Delta Y}{\Delta X}\right]\right] - Y\sin\left[\tan^{-1}\left[\frac{\Delta Y}{\Delta X}\right]\right], \tag{14}$$

and

$$Y_c = Y\cos\left[\tan^{-1}\left[\frac{\Delta Y}{\Delta X}\right]\right] + X\sin\left[\tan^{-1}\left[\frac{\Delta Y}{\Delta X}\right]\right]. \tag{15}$$

A similar method of data correction was employed by Costescu *et al.*[13] to correct the data for radial diffusion in the substrate. In practice, the phase of the lock-in is adjusted before each measurements so that Y is constant as the stage moves across $\tau = 0$[36] so that Eq. (14) and (15) can be used simply as a check to ensure that the phase adjustment has removed the majority of the instrument noise. This also allows for the instrument noise to be quantified in terms of the lock-in phase so that this adjustment can be used in future measurements and analysis.[47]

To evaluate the various thermophysical properties of interest, we must determine an appropriate range in which to fit the various models to the experimental data. For example, a given material system may be extremely sensitive to changes in h_K over a certain range but not κ. This aspect of the models is used to determine ranges in which to fit the various models to the data. Costescu *et al.*[13] defined a sensitivity factor as

$$S_p = \partial \ln\left[-\frac{X}{Y}\right] \Big/ \partial \ln[p], \tag{16}$$

where p is some thermophysical property of interest. To determine the sensitivity of h_K or κ over the pump probe delay time in the TDTR data, we perturb the value of h_K or κ by 1% in calculations of Eq. (16) so effectively our sensitivity becomes

$$S_p = 100\frac{Y}{X}\partial\left[\frac{X}{Y}\right], \tag{17}$$

where the derivative of the ratio is estimated by subtracting the model calculations from the perturbed model calculations. Figure 4 shows the sensitivities of the thermal transport from TDTR as a function of pump probe delay time for a 100 nm Al film on Si and SiO_2 substrates at room temperature assuming a 15 μm pump and probe spot size. In the sensitivity calculations, the thermal boundary conductance is taken as 200 MW m^{-2} K^{-1} for Al/Si and 50 MW m^{-2} K^{-1} for Al on SiO_2.[34,48] We use literature values for the thermal properties of the Al, Si, and SiO_2.[49] There are two aspects of the sensitivity curve that are important when fitting the model to the TDTR data, the magnitude and the curvature. An optimal sensitivity curve will exhibit a large magnitude and variance over the pump-probe delay time. For example, the sensitivity to the thermal conductivity of the Si substrate is ideal since it is relatively large and very dynamic compared to that of SiO_2. The sensitivity to h_K across the Al/Si interface is also appealing but loses sensitivity around 500 – 1,000 ps. Note that the sensitivity of the model in the Al/SiO_2 system is primarily due to the thermal conductivity of the substrate. For low thermal conductivity structures, this is powerful if only the thermal conductivity needs to be determined and not h_K since it reduces the number of free parameters in the fit. We do not include the sensitivity to the Al film thermal conductivity since the TDTR measurements are nearly

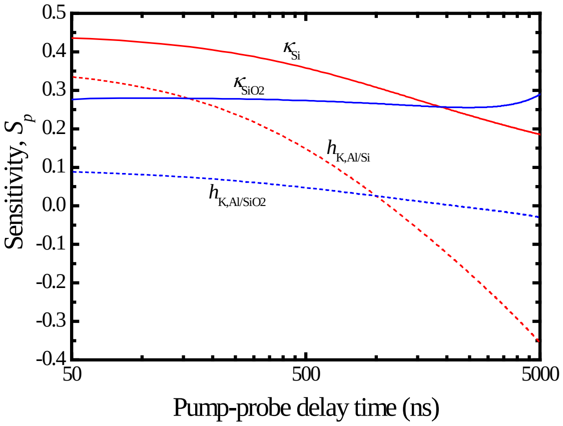

Fig. 4. Thermal sensitivities in TDTR to h_K and κ of the substrate in 100 nm Al/Si and Al/SiO_2 systems.

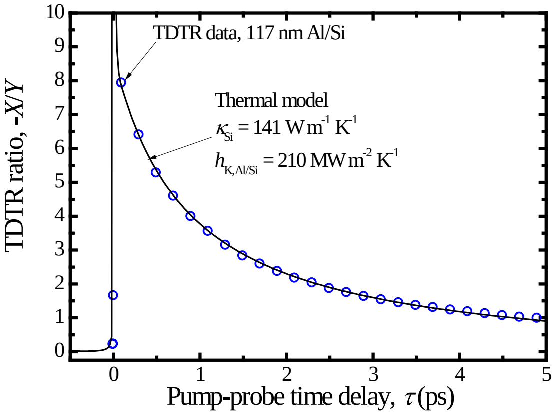

Fig. 5. TDTR data from a 117 nm Al film evaporated on a Si substrate along with the best fit from the thermal model. The thermophysical properties determined from the model best fits are h_K = 210 MW m^{-2} K^{-1} for the Al/Si interface and κ = 141 W m^{-1} K^{-1} for the Si substrate.

insensitive to this parameter over the majority of the pump-probe time delay. Assuming a diffusivity of Al as D = 97.1x10^{-6} m^2 s^{-1}, the time it takes for the heat to diffuse through the film is given by $\approx d^2/D$ where d is the film thickness.[49] For a 100 nm Al film, the thermal energy has fully diffused through the film thickness after only 100 ps.

TDTR data on a 117 nm Al film evaporated onto a single crystalline, lightly doped Si substrate are shown in Fig. 5 along with the best fit from the thermal model. The thermal conductivity of the 117 nm Al film is 200 W m^{-1} K^{-1} as determined from electrical resistivity measurements and the Wiedemann-Franz Law. Although this procedure for determining the Al thermal conductivity is really a measure of in-plane conductivity where the model requires cross plane, since the Al film is polycrystalline, it is valid to assume that the in-plane and cross plane conductivities are equivalent for an approximately 100 nm Al film. The thickness of the Al film was measured with picosecond ultrasonics, another powerful aspect of this TDTR experimental setup.[50,51] The thermal model, which accounts for pulse accumulation and radial spreading, is fit to the data by adjusting $h_{K,12}$ and κ_2. The data shown here are the real component of the lock-in signal divided by the imaginary component; i.e., $-X/Y$. This approach of normalizing the signal by the imaginary component of the voltage cancels out detection noise and makes the signal insensitive to various experimental parameters that can be difficult to account for during data analysis.[36] This approach is the same as using the phase of the signal.[29,35] Note that analyzing the ratio (i.e., $-X/Y$) also removes the requirement of scaling the model to the data, thereby giving more sensitivity in the fit to various thermophysical parameters.

4. REPRESENTATIVE RESULTS

This LDRD has resulted in 39 refereed journal publications, with an additional 2 publications currently under review and 1 invited book chapter. This Section discusses only a few of the results reported in these publications in depth. A full list of all the journal publications is given in the Appendix.

4.1. Controlling thermal conductance through quantum dot roughening at interfaces (Hopkins, Duda, Petz, and Floro, *Physical Review B* 84, 035438 (2011)).

Successful reductions in the thermal conductivities of nanosystems have been achieved through the alteration of structure and interface density in different types of nanoparticle films and periodic composites.[6,31,32,52-61] These material systems have attracted significant attention due to their unique phonon-scattering mechanisms, where the increase in the density of inclusions increases the number and frequency of boundary scattering events, in turn resulting in lower realized values of effective thermal conductivity. Thus, through varying the frequency and strength of phonon scattering at interfaces, one is able to obtain a unique method for controlling the effective thermal conductivity of a given nanosystem. This concept is of great interest for applications involving thermoelectric cooling and power generation,[62-64] and thermal insulation.[65]

Recent investigations have examined the effects of SiGe-based quantum dot (QD) superlattices in an attempt to further reduce the thermal conductivities of SiGe material systems.[6,66,67] These efforts have collectively determined that QD patterning at interfaces drastically reduces the overall thermal conductivity of SiGe superlattice materials. The recent work by Pernot *et al.*[6] further demonstrated the "tunability" of this reduction in thermal conductivity by precise control over superlattice period and QD areal density. They attributed this control to diffusive scattering at the QD-covered interfaces. However, the notion of diffusive interface scattering largely encompasses a broad domain of phonon transport processes. Therefore, the fundamental phononic mechanisms driving the reduction in the cross plane thermal conductivity of quantum dot superlattices remain controversial[67] and include acoustic impedance mismatch scattering, phonon localization and attenuation, and alteration of phonon dispersion relations.[3]

In this work, we examine fundamental phonon mechanisms affecting the thermal conductance of QD-superlattices by studying the thermal boundary conductance, or Kapitza conductance (h_K), across a single layer of QDs on a planar substrate. We synthesize a series of $Ge_xSi_{(1-x)}$ QDs by heteroepitaxial self-assembly on Si surfaces and metallize (aluminum) the surface to study how the QDs affect the heat transport across interfaces. Growth conditions are modified to provide QD layers with different RMS roughness levels in order to quantify the effects of roughness on thermal transport. We measure the thermal boundary conductance with time-domain thermoreflectance (TDTR).[36,48] The trends in thermal boundary conductance show that the effect of the QDs on h_K are more apparent at elevated temperatures, where at low temperatures, the QD patterning does not drastically affect h_K. The functional dependence of h_K with RMS surface roughness reveals a trend that suggests that both vibrational mismatch and phonon attenuation near the interface contribute to the reduction in h_K. We develop an analytical model for phonon thermal transport across rough interfaces based on a diffusive scattering assumption and phonon attenuation that describes the measured trends in h_K. This indicates that

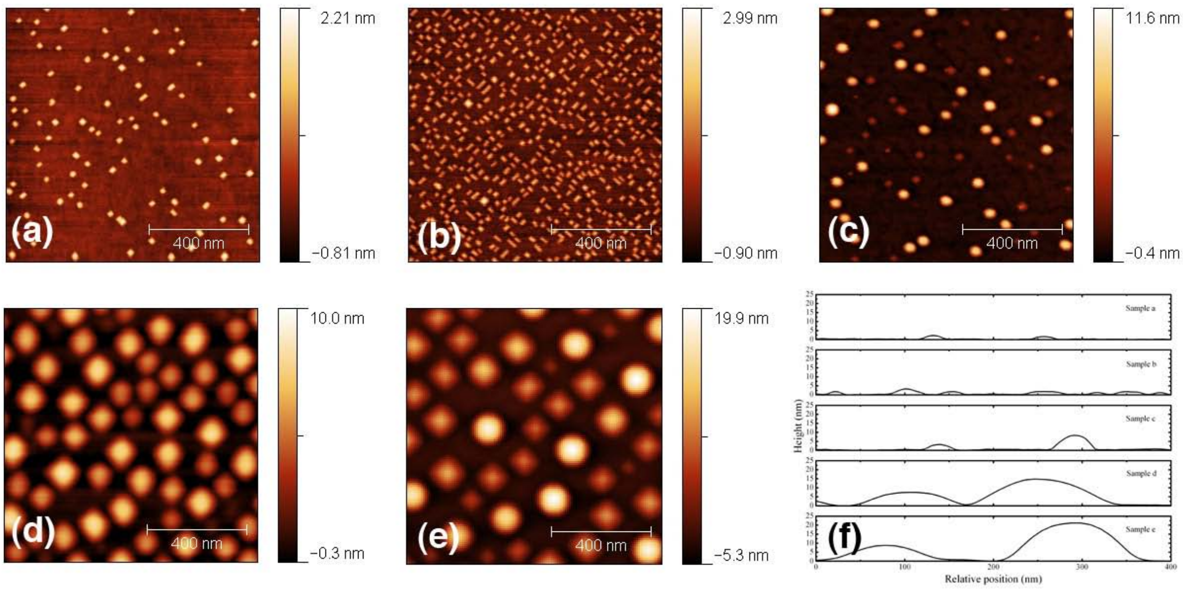

Fig. 6. Atomic force microscrope images and representative line scans of the QD roughened surfaces studied in this work. These specific surfaces have RMS roughnesses of (a) 0.28 nm from Ge QDs, (b) 0.53 nm from Ge QDs, (c) 1.38 nm from Ge QDs, (d) 2.16 nm from GeSi QDs, and (e) 4.46 nm from GeSi QDs. The representative line scans of each AFM are shown in (f).

the observed reduction in thermal conductivity in SiGe superlattices is primarily due to the increased physical roughness at the interfaces, which creates additional phonon resistive mechanisms beyond the interfacial vibrational mismatch.

The growth of the various QD-roughened Si surfaces begins with heteroepitaxial growth of $Ge_xSi_{(1-x)}$ via the Stranski-Krastanow growth mode.[68] The alloy layer initially grows planar on the Si(001) surface, but above some wetting layer thickness, subsequent material forms coherent 3D islands to partially relieve the lattice mismatch strain (given by $\varepsilon_{\mathrm{mis}} = 0.04x$). Initially, “pyramid” islands form exhibiting four-fold symmetric {105} facets, and with continued GeSi deposition, larger “dome” shaped islands evolve with dominant {113} facets.[69-71] Pyramid and dome size and areal density may be modified (thereby varying the surface roughness) by controlling the composition, film thickness and growth kinetics, e.g., substrate temperature and deposition rate.[72,73]

$Ge_xSi_{(1-x)}$/Si(001) QDs are grown via ultra-high vacuum molecular beam epitaxy (MBE) (base pressure = 10^{-10} Torr). Prior to insertion to the MBE, Si wafers are chemically cleaned via a standard IMEC/Shiraki process to remove hydrocarbon and transition metal impurities, creating in the final step a passive SiO_x layer. Si(001) substrates, with a miscut of +/- 0.1º, are outgassed in the MBE at 600ºC for greater than 10 hrs, ramped to 850ºC over 30 min to desorb the oxide layer, and cooled to 700ºC for deposition of a 50 nm Si buffer layer. Throughout this process, the surface structure is monitored with reflection high energy electron diffraction (RHEED) to ensure 2x1 surface reconstruction. We deposit Ge and Si with magnetron sputtering in 3 mTorr of getter-purified Ar. Once a clean surface is obtained, Ge(GeSi) heteroepitaxy proceeds. After growth, surface morphology is characterized *ex-situ* by atomic force microscopy (NT-MDT Solver Pro M) using NSG10 tips with radius less than 10 nm. The observed surface features from atomic force microscopy micrographs, and representative line features for each film are shown in Fig. 6. The representative line scans are taken around the vicinity QDs to make clear

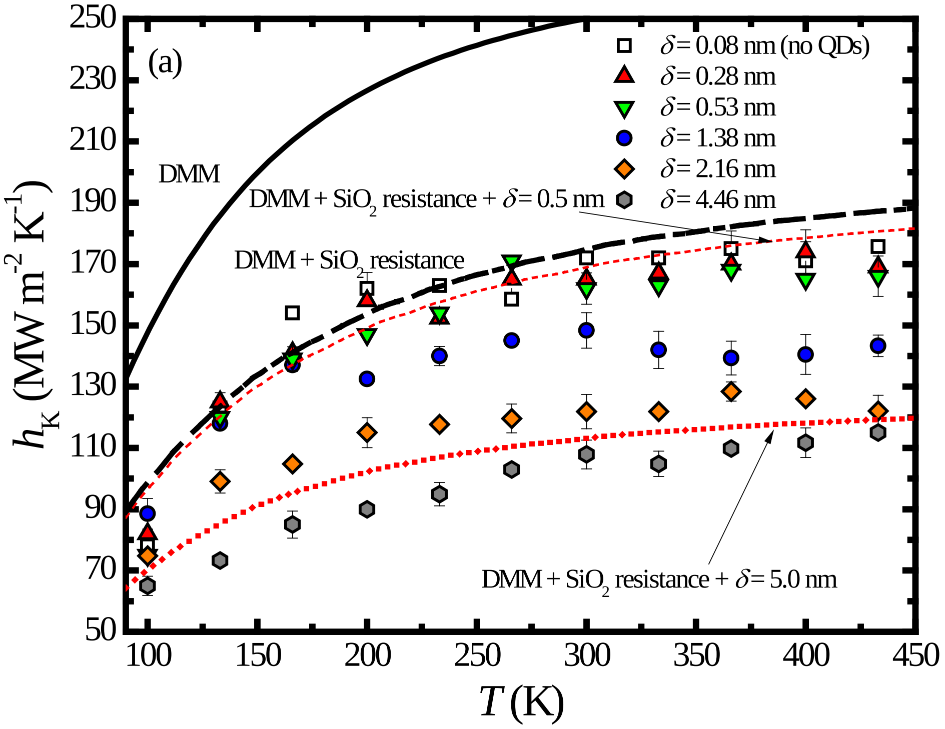

Fig. 7. Measured thermal conductance of the six Al/Si interfaces fabricated in this work as a function of temperature. The QD patterning on the surface of the Si causes reduction in h_K. In addition, the measured h_K on the six samples converges at low temperature indicating that phonons are not as readily affected by the roughness at low temperatures, indicative of longer-wavelength phonon-dominated transport. Also shown in this figure are calculations of the DMM. Including the thermal resistance associated with the native oxide layer on the surface of the Si greatly improves the agreement between the DMM and the Al/Si interface with no QD patterning. The roughness is accounted for by assuming that short wavelength phonons are more readily scattered at rough interfaces that have greater coverage of QDs, as described by Eq. (25). We plot the DMM using the phonon attenuation parameter given in Eq. (25) as the dashed lines assuming an QD RMS roughness of δ = 0.5 nm or 5.0 nm. Our model that accounts for additional scattering by the QD's agree well in both value and trend as the corresponding data with similar RMS roughnesses.

the difference in surface features among the different samples. RMS roughness values (δ) are calculated from the AFM micrographs and represent less than 4% error. Prior to metallization, we clean the substrate with methanol and acetone and dry with nitrogen. We then evaporate 90 nm of Al on the QD-roughened Si surfaces at a vacuum pressure of 3.7 x 10^{-7} Torr. We measured the thermal boundary conductance across the QD-structurally variant Al/Si interfaces with TDTR, which is detailed in Section 3.

Figure 7 shows the measured thermal conductance across the various Al/Si interfaces as a function of temperature, T. The control sample (no QD patterning, δ = 0.08 nm) has the highest conductance. The general trend amongst the data indicate that the conductance decreases due to the physical surface roughness associated with the QD topography, even at surface roughnesses less than 1 nm. Also, note that the values for conductance converge at low temperatures. This is due to the fact that the magnitude of the surface roughness selectively scatters only certain phonons with wavelengths less than the characteristic roughness produced by the QD's, a potential avenue for control of thermal interface conductance based on the magnitude of the roughness. These phonon scattering mechanisms at these rough QD interfaces are quantified and discussed in the remainder of this paper.

To better understand phonon transport across roughened interfaces, we turn to interfacial modeling via the diffuse mismatch model (DMM).[12] The DMM makes the assumption that all phonons approaching an interface between two materials must scatter diffusively. The drastic change in lattice periodicity from one material to another will cause scattering at the interface, thereby restricting phonon mean free paths to the interfacial scattering events. The diffusive nature of this interfacial scattering event is justified at elevated temperatures ($T > 50$ K) due to phonon wavelength considerations.[74] For DMM calculations, we use the exact phonon dispersion in a given crystallographic direction and employ an isotropic assumption when describing the phononic properties of Al and Si.[74] That is, we assume isotropic dispersion based on that in the [100] direction for both Al and Si from Refs. 75 and 76, respectively. We have previously shown that this isotropic dispersion assumption is acceptable for predicting interface conductance across junctions between cubic crystals and yields a much improved prediction over traditional Debye approaches.[74] Under the isotropic assumption, the phonon flux cross the interface from the Al to the Si is given as

$$q_{1\to 2} = \frac{1}{8\pi^2}\sum_j \int_{k_{1,\max}} \hbar\omega_j\left(k_1\right)k_1^2\zeta^{1\to 2}\left|v_{1,j}\left(k_1\right)\right| n\, dk_1 \,, \tag{18}$$

where k is the wavevector, $k_{\max}$ is the maximum wavevector, ω is the phonon angular frequency, $\zeta^{1\to 2}$ is the transmission probability from side 1 (Al) to side 2 (Si), v_1 is phonon group velocity in the Al and equal to $\partial\omega/\partial k$, n is the phonon distribution function, which in this work we assume as the equilibrium Bose-Einstein distribution, and j is polarization (e.g., longitudinal acoustic or transverse acoustic). Recognizing that $q_{1\to 2} = h_{\mathrm{K}}\Delta T$, the thermal boundary conductance is given by[77]

$$h_{\mathrm{K},1\to 2} = \frac{1}{8\pi^2}\sum_j \int_{k_{1,\max}} \hbar\omega_j\left(k_1\right)k_1^2\zeta^{1\to 2}\left|v_{1,j}\left(k_1\right)\right| \frac{\partial n}{\partial T}\, dk_1 \,. \tag{19}$$

We assume that the phonons are scattered elastically at the interface[74] so that frequencies only up to the maximum frequency in Al are considered. To calculate the transmission coefficient, we apply detailed balance on the fluxes crossing the interface from the Al and from the Si and apply the definition of diffuse scattering (i.e., $\zeta^{1\to 2} = 1-\zeta^{2\to 1}$) to yield[74]

$$\zeta^{1\to 2} = \frac{\sum_j k_2^2}{\sum_j k_1^2 + \sum_j k_2^2}\,, \tag{20}$$

where the transmission at each phonon frequency, regardless of polarization, is calculated consistent with our assumptions during application of detailed balance and calculation of Eq. (19), namely, elastic scattering.[78] Therefore, under the isotropic and diffuse assumptions, h_{K} as calculated via the DMM is given as

$$h_{\mathrm{K},1\to 2} = \frac{1}{8\pi^2}\sum_j \int_{k_{1,\max}} \hbar\omega_j\left(k_1\right)k_1^2 \frac{\sum_j k_2^2}{\sum_j k_1^2 + \sum_j k_2^2}\left|v_{1,j}\left(k_1\right)\right| \frac{\partial n}{\partial T}\, dk_1 \,. \tag{21}$$

The calculations of the DMM as a function of temperature are labeled as “DMM” in Fig. 7. These predictions clearly overestimate the measured data on our smoothest sample with no QD patterning. Another resistance that must be accounted for at these interfaces is the resistance associated with the native oxide layer on the sample surface. In our previous work,[22] we determined that the thermal resistance associated with the native oxide can be approximated as the thickness of the native oxide layer divided by the thermal conductivity of corresponding amorphous bulk phase. The conductance of this layer is then

$$h_{\mathrm{oxide}} = \frac{\kappa_{\mathrm{oxide}}}{d_{\mathrm{oxide}}}. \tag{22}$$

where d is the native oxide layer thickness and we assume the thermal conductivity of the native oxide layer is given by that of bulk SiO_2,[79] so that the effective conductance of the Al/Si interface with a native oxide layer on the sample surface is given by

$$h_{\mathrm{K}} = \left(h_{\mathrm{K,DMM}}^{-1} + h_{\mathrm{oxide}}^{-1}\right)^{-1}. \tag{23}$$

Note that for these calculations we use the thermal conductivity of SiO_2. Although there may also be some formation of germania in the native oxide layer, the thermal conductivity of vitreous Si and Ge are similar at elevated temperature[80] so germania in the native oxide layer should not significantly affect our calculations. The DMM predictions when accounting for a native oxide layer are in much better agreement with our Al/Si interface than the corresponding predictions without the native oxide layer resistance. The increase at higher temperatures in the model is due to our assumption that the SiO_2 conductance follows the temperature dependency of thicker, amorphous SiO_2. However, the agreement between our DMM calculations and our measured Al/Si interface conductance suggests that the DMM is a suitable model to explore the phonon processes participating in thermal conductance at Al/Si interfaces in the temperature range of interest in this work. Furthermore, this suggests that phonons are scattering diffusely at the temperatures of interest in this study and the interface conductance is driven by the vibrational mismatch between the Al and Si which manifests itself as a mismatch of phonon density of states. However, the DMM with the additional native oxide resistance does not explain the variation in h_{K} that we observe with QD patterning and roughness.

In this work, our $Ge_xSi_{(1-x)}$/Si materials and interfaces are fully crystalline and coherent, but covered by a native oxide. The Al layer is polycrystalline, but intermixing is suppressed by the low growth temperature and the presence of the SiO_2. Thus, we take the view that the self-assembled quantum dots affect thermal boundary conductance only via mechanisms induced by the topographic roughness, but do not otherwise have a unique vibrational identity. We discuss the veracity of this assumption later. Previous works have modeled phonon transport across heterointerfaces incorporating non-idealities such as extended chemical intermixing,[21,22,24] misfit dislocations,[19,81] and microcrystalline or amorphous regions.[21,22,25,82] In all of these previous works, changes in h_{K} were controlled by changes in the diffusive phonon scattering events around the interface caused by these non-idealities.

To account for the various scattering events at the QD-patterned interfaces, we introduce an “attenuation-type” model, similar to the Beer-Lambert law of photon attenuation. In this case, we introduce a roughness factor, γ, in the thermal boundary conductance in Eq. (21), so that the DMM is calculated by

$$h_{\mathrm{K},1\rightarrow 2} = \frac{1}{8\pi^2}\sum_j \int_{k_{1,\max}} \gamma\hbar\omega_j\left(k_1\right)k_1^2 \frac{\sum_j k_2^2}{\sum_j k_1^2 + \sum_j k_2^2}\left|v_{1,j}\left(k_1\right)\right|\frac{\partial n}{\partial T}\,dk_1 . \tag{24}$$

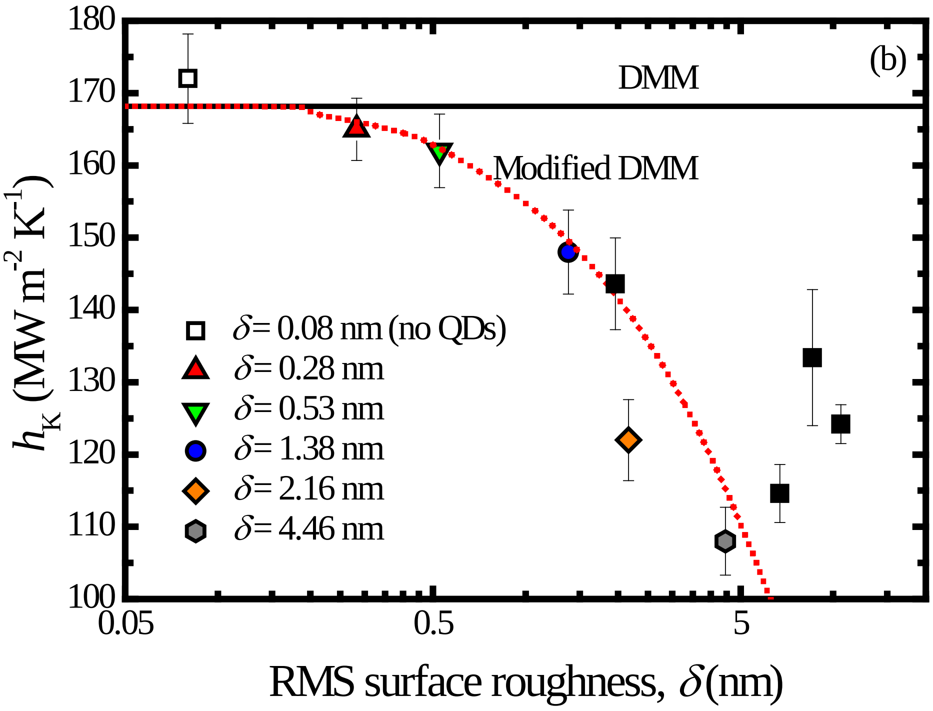

Fig. 8. Thermal conductance as a function of RMS roughness across the series of structurally variant Al/Si interfaces at 300 K. Calculations of Eq. (24) at T = 300 K as a function of δ are also shown. We find that β = 0.0040 leads to a good agreement between the model and experimental data.

In Eq. (24), γ accounts for the geometric roughness of the interface and is related to the phonon attenuation events due to the finite roughness. We define this roughness factor as

$$\gamma = \begin{cases} 1 & \lambda > \delta \\ \exp\left[-\dfrac{4\pi\beta}{\lambda}\delta\right] & \lambda < \delta \end{cases}. \tag{25}$$

where λ is the phonon wavelength and we define β as the unitless phonon attenuation constant of the interface (for a perfect interface, $\beta \to 0$), and δ is the RMS roughness of the interface. Note that the phonon wavelength, λ, is a related to the phonon wavevector, k, and therefore this expression is inserted into the integrand of Eq. (24). In Eq. (25), the term $4\pi\beta/\lambda$ exactly parallels the linear attenuation coefficient of photons as described by the Beer-Lambert law. The piecewise definition of the model describes a scenario in which phonons with wavelengths longer than δ do not see the rough region, and therefore their interfacial conductance is governed by that predicted by the DMM. On the other hand, the degree to which phonons with wavelengths shorter than δ are attenuated by this region depends on the relative values of λ and δ, and the phonons propagating in this region are attenuated by γ. This wavelength dependency of thermal boundary conductance has been previously observed at grain boundaries with only a few monolayers of roughness using molecular dynamics simulations.[83]

To examine the effect of interface roughness on h_K, we plot h_K as a function of δ at 300 K for the six samples measured in this study in Fig. 8. Calculations of Eq. (24) at T = 300 K as a function of δ are also shown in Fig. 8. Note that in these calculations we also account for the native oxide layer via Eq. (23). We use β as a fitting parameter to account for the various scattering mechanisms at the QD patterened interfaces that can be leading to phonon attenuation. We find that a single value of $\beta = 0.0040$ leads to a good agreement between the model and experimental data, indicating that phonons are being attenuated by similar mechanisms at the various Al/QD/Si interfaces. The model given in Eqs. (24) and (25) assumes that phonons are diffusely scattered at the Al/Si interface via processes described by the DMM. It also accounts for the interfacial flux that is additionally attenuated by the scattering of short wavelength phonons via the structure around the interface. This short wavelength phonon attenuation drives the trend in h_K with interfacial roughness. Note that the material comprising the interface structure, i.e., Ge or GeSi, does not enter into the formulation of this model. This indicates that the heat flow is strongly dictated by the differences in the phonon density of states between the Al and the Si, while topographical roughness at the interface causes additional phonon attenuation and localization. The excellent fit to the data indicates that the limited amount of Ge on the Si surface does not have a vibrational identity distinguishable from that of the substrate.

We also show predictions of Eq. (24) for an RMS roughness of 0.5 and 5 nm in Fig. 7 assuming $\beta = 0.0040$; these predictions capture the temperature dependent reduction in h_K due to roughness relatively well with a single value of β. In addition, note that the roughness models begin to converge at low temperatures - a similar trend as is observed in the experimental data. This is due to the fact that, at low temperatures, the thermal flux has a higher population of phonons with wavelengths greater than δ as compared to elevated (room) temperatures; consequently, these long wavelength phonons do not “see” the interfacial features and are scattered from DMM-type considerations alone (i.e., mismatch in phonon density of states). We note that this sound agreement between our data and this attenuation-based phonon transport model is achieved with only one fitting parameter. This idea of interfacial phonon attenuation is captured with our relatively simple, analytical model and agrees well with our quantum-dot-roughened interfaces, despite the fact that these interfaces exhibit a wide range of lateral length scales and represent nanostructured roughness rather than random atomic roughness.

To further validate this model, we use this description of phonon attenuation to predict the effective thermal conductivity of a QD superlattice as measured by Pernot *et al.*[6] The Ge QD-patterned Si/Si interfaces in that study were characterized as having a 70% QD coverage area with an average feature height of 1.2 nm, corresponding to an RMS roughness of approximately 1 nm. According to our above description of phonon transport at QD-patterned interfaces, the Ge QD arrays at each interface do not have significant vibrational identities of their own. Therefore, we calculate our predictions of interface conductance for a single Ge QD-patterned Si/Si interface using the same bulk phonon dispersion of Si described above.[76] We use $\beta = 0.0040$ to stay consistent with our above calculations. At room temperature, the model predicts an individual interface conductance of 255 MW m^{-2} K^{-1} at 300 K, which is in excellent agreement with the value inferred by Pernot *et al.* (between 250 and 500 MW m^{-2} K^{-1}). Assuming the bulk thermal conductivity of Si at 300 K, $\kappa_{\mathrm{Si}} = 148$ W m^{-1} K^{-1}, and using the described interface spacing d, where $d = 12.8$ nm, an effective thermal conductivity can be calculated through consideration of the individual conductances (interface and bulk) and the effective length scale, d, given by

$$\kappa_{eff} = L\left[h_{\mathrm{K}}^{-1} + \left(\frac{\kappa_{Si}}{L}\right)^{-1}\right]^{-1}. \tag{26}$$

Equation (26) yields $\kappa_{eff} = 3.2$ W m^{-1} K^{-1} at 300 K, which is again in excellent agreement with the two reported measurements of Pernot *et al.*, 3.7 ± 0.85 W m^{-1} K^{-1} and 3.4 ± 0.50 W m^{-1} K^{-1}.

The fact that a single attenuation constant accurately describes phonon transport across the various silicon interfaces in this work and that of Pernot *et al*.[6] lends insight into the phonon scattering processes driving thermal boundary conductance at roughened interfaces. The attenutation coefficient for phonons introduced in this work, given by $4\pi\beta/\lambda$, exactly parallels its photonic counterpart thereby representing the total loss of the phonon flux at the interface. For phonons, this represents additional scattering events that restrict the heat flow across the interface. Given the rough features from QD synthesis on a Si surface, the incident phonon flux is affected by the mismatch between the phonon flux and the phonon density of states in the Si and further attenuated by the presence of vibrationally unidentifiable features at the interface. As the phonon attenuation exists only at a few nanometers around the interface, this implies that the roughened features localize the phonon scattering near the interface, indicating that both phonon localization effects and vibrational mismatch between two materials are the fundamental phononic mechanisms driving the reduction in the cross plane thermal conductivity of quantum dot superlattices.

In summary, in this work we find that QD roughening at Si interfaces decreases the thermal conductance via localized phonon scattering events beyond vibrational mismatch resistance. The trends in thermal boundary conductance between Al and Si show that the effect of the QDs on phonon scattering are more apparent at elevated temperatures, where at low temperatures, the QD patterning does not drastically affect h_K. We find that QD structures with RMS roughness greater than 4 nm decrease h_K at Si interfaces by a factor of 1.6. We develop an analytical model for phonon scattering at rough interfaces showing that the observed reduction in the cross plane thermal conductivity of QD superlattices is due to diffusive scattering driven by vibrational mismatch and phonon localization at the superlattice interfaces.

4.2. Manipulating thermal conductance at metal-graphene contacts via the chemical modification of graphene (Hopkins, Baraket, Barnat, Beechem, Kearney, Robinson, and Walton, *currently under review*).

Graphene-based devices have garnered tremendous attention due to the unique physical properties arising from this purely two dimensional carbon sheet.[84,85] These unique properties allow for tremendous efficiency in the transport of not only charge carriers but also thermal carriers (i.e., phonons) as well. [18,86-89] For these reasons, graphene is being pursued both for a myriad of electronic applications and as an enabler of next generation thermal solutions. In either case, it is necessary for this two-dimensional material to be able to efficiently transport heat into the surrounding 3D device architecture in order to fully capitalize on its intrinsic transport capabilities. Therefore, heat flow across solid-graphene interfaces, which is governed by the thermal boundary conductance,[12] or Kapitza conductance,[90] h_K, is a critical parameter in the realization of graphene electronics and thermal solutions.

To this end, previous groups have measured h_K at SiO_2/graphene (Ref. 16) and Au/graphene/SiO_2 interfaces (Ref. 18). The SiO_2/graphene interface exhibited a thermal boundary conductance approaching that of a typical metal/nonmetal interface at room temperature (~100 MW m^{-2} K^{-1} – Ref. 91). In contrast, the Au-graphene interface demonstrated a thermal boundary conductance at room temperature that was nearly a factor of 2 lower (Refs. 18 and 92). This discrepancy, in turn, can be explained utilizing traditional phonon scattering models (e.g., diffuse mismatch model (DMM)[93]) in which the lower conductance at the Au

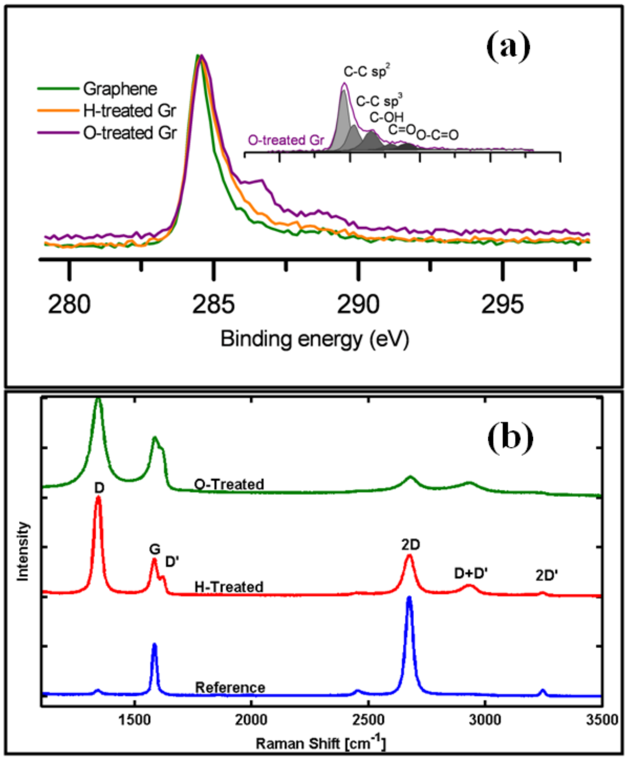

Fig. 9. (a) High resolution C1s spectra of untreated graphene and plasma treated graphene. The inset shows the oxygen treated sample along with peak fitting results. (b) Averaged Raman spectra for each of the films analyzed in this study. While the reference film shows a high level of crystallinity, functionalization induces nanocrystallinity in the H-treated film, and begins to induce amorphous regions of sp^3 carbon in the oxygen treated film.

boundary is attributed to Au having a lower energy cutoff of available modes to transport energy as compared to both the graphene and SiO_2. While this theory is supported in part by investigations of metal/graphite interfaces, chemical bonding between the layers has been shown to play a prominent role in phonon transmission, and thus h_K, as well.[94] In spite of this fact, the interplay between chemical bonding, the allowable phonon modes, and the subsequent effect on interfacial thermal transport remains unclear. For graphene boundaries, meanwhile, the material's inherent surface sensitivity will only enhance this interplay.

In response, we investigate the role of interfacial bonding at metal/single layer graphene (SLG) interfaces by introducing chemical adsorbates on the SLG surfaces in order to increase the density of covalent bonds bridging the metal and the SLG. In doing so, we demonstrate plasma-based funtionalization of graphene surfaces as a means to manipulate the thermal boundary conductance. Specifically, we metalize plasma functionalized graphene and then measure h_K at Al/SLG/SiO_2 contacts with time domain thermoreflectance (TDTR) techniques.[36,48] Through these measurements, adsorbates on the SLG surfaces are shown to influence the cross plane thermal conductance. These influences are attributed to changes in the bonding between the metal and the SLG that itself is affected by increased disorder within the SLG. Additionally, the Al/SLG/SiO_2 thermal boundary conductance is shown to be comprised of two separate conductances – Al/SLG and SLG/SiO_2 – in line with the conclusions from Ref. 18. Using our measured values of h_K in conjunction with previous measurements between metals and carbon-based materials,[18,94] the thermal boundary conductance is found to be most influenced by the interfacial chemical bonding as both the phonon flux and the vibrational mismatch between the materials are each subject to the to the interfacial bond strength.

The graphene films were grown by chemical vapor deposition on Cu substrates and transferred to SiO_2/Si substrates using the conventional wet chemical approach.[95] The graphene films were then functionalized with oxygen and hydrogen using electron beam generated plasmas[96] produced in Ar/O_2 and Ar/H_2, respectively. The functionalization process leads to an inclusion of chemical moieties on the graphene surface, which was verified by X-ray Photoelectron Spectroscopy (XPS). The total oxygen present on the surface after treatment in the oxygen containing plasma is ~ 25 at.%. A careful inspection of the C1s peak reveals the presence of hydroxyl and carboxyl groups as indicated by the well pronounced peaks around 286.6 eV and 289 eV (Fig. 9a). Although the presence of hydrogen cannot be quantified by XPS, the broadening of the main peak (located at 384.5 eV) indicates the increase of sp^3 hybridized carbon atoms, which is mainly attributed to the incorporation of hydrogen. From the fitting procedure, the contribution from the sp^3 peak (situated at +0.65 eV from main peak) increased from 22% for graphene to ~33% for H-treated graphene (Fig. 9a).

To structurally characterize the graphene films, we perform Raman spectroscopy on the functionalized samples along with a reference film. In each case, Raman spectra are acquired using a 532 nm laser light across a 15x15 µm with individual acquisitions separated by 333 nm. Laser powers were not found to damage the sample. Using the FWHM of 2D mode at ~2678, each of the films are found to be composed almost completely composed of SLG.[97] As very little difference in the character of the graphene is found across the sample, each of the SLG spectra are averaged and shown in Fig. 9b.

Before functionalization, the graphene films contain very little disorder as the ratio of the D-Band (~1350 cm^{-1}) intensity to that of the G-Band (~1580 cm^{-1}) is, I(D)/I(G)~0.2. Significant levels of disorder become apparent, however, upon exposure to either the oxygen or hydrogen plasma. Such disorder is readily apparent in each film through the increased intensities of several spectral features (e.g., D, D', and D+D' modes) that are directly indicative of a reduction in the periodicity of the lattice. While both functionalized films do exhibit disorder, the extent of this disorder is substantially different between the films. In the hydrogen exposed film for example, the 2D peak and the G-peak have much greater intensities that the D+D' peak and the D' peak, respectively. A spectrum of this character is indicative of graphene that has become nanocrystalline.[98] Whereas the G-peak and 2D peak have much greater intensities in comparison to the D' and D+D' in the hydrogen exposed samples, these peaks have similar intensities relative to one another for the film exposed to an oxygen plasma. A spectrum of this form, in turn, indicates that the graphene has progressed from being nanocrystalline to one in which there is at least a small degree of amorphous sp^3 character.[98] To quantify these differences, the mean distance between the point defects induced by the functionalization is calculated using Eq. (1) from Ref. 98. Using this approach, distances of 28, 6, and 2 nm are found for the reference, hydrogen, and oxygen exposed films respectively. Most simply, the disorder increases as one moves from the reference to the hydrogen and then finally the oxygen. Finally, it is of note that these changes do not alter the strain state[99] or carrier concentration[100] between the films as each are found to have peak positions of the G and 2D bands that are within the spectrometer resolution of +/- 1 cm^{-1}. Thus, any induced changes in the heat transport are a consequence of the bonding/defect states of the film and not due to strain or carrier effects.

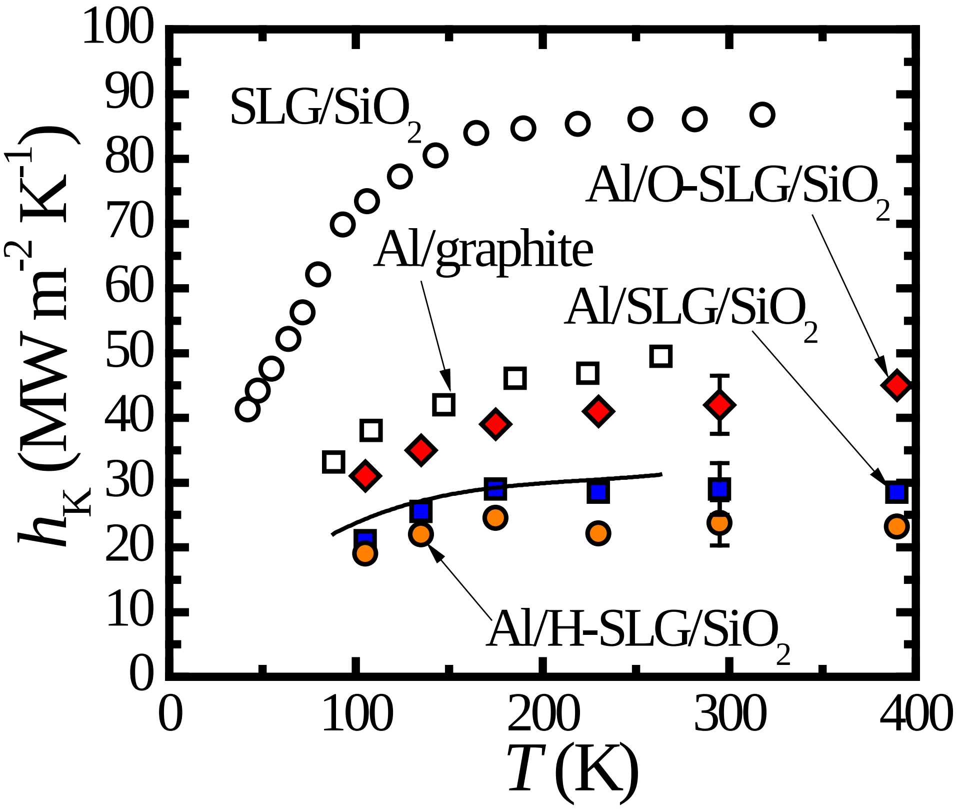

Fig. 10. Measured thermal boundary conductances on the Al/SLG/SiO$_2$ sample (filled squares), the hydrogen functionalized sample (filled circles), and the oxygen functionalized sample (filled diamonds). The hydrogen functionalization process, which introduces disorder on the SLG, also leaves the SLG surface chemically inert and does not leave any additional bonding mechanism for the Al to the SLG. The slight decrease in h_K that we observe due to hydrogen functionalization is therefore due to the disorder at the Al/SLG interface. Functionalizing the SLG with oxygen leaves the graphene surface reactive leading to increased covalent bonds linking the Al to the SLG, which results in a higher phonon transmission and increase in h_K. For comparison, we also show h_K across SLG/SiO$_2$ (open circles – Ref. 16) and Al/graphite (open squares – Ref. 94) interfaces. Using these two measured conductances with Eq. (1), we can predict the Al/SLG/SiO$_2$ interface assuming that the Al/graphite h_K is similar to Al/SLG and that the Al/SLG and SLG/SiO$_2$ conductances can be separated. The resulting conductance, which is depicted by the solid line, is in very good agreement with our Al/SLG/SiO$_2$ measurements, indicating that the Al/SLG/SiO$_2$ thermal boundary conductance can be described by two separate conductances – Al/SLG and SLG/SiO$_2$.

Prior to TDTR measurements, we metalize each sample with 90 nm of electron beam evaporated Al at base pressures no greater than 2.3x10^{-7} Torr. We then measure the thermal boundary conductance across the Al/SLG/SiO$_2$ interfaces with TDTR.[44] It is possible that using this technique bi-layer graphene could be sampled instead of SLG since the metal film inhibits the ability to identify layer number using established techniques. To compensate for this possibility, we perform several TDTR scans at different locations of two different samples of each sample type (7 – 10 scans total for each type of graphene sample). Typical uncertainties due to the different locations on the samples or from sample to sample were less than 10% (calculated from the standard deviation among all the TDTR scans on a given sample type), which is smaller than the variation in metal/graphene/SiO$_2$ h_K expected due to a transition from SLG to *n*-layer graphene where $n > 1$ (~25 – 35%), as measured via TDTR.[18] This indicates that our samples were primarily SLG, confirming our Raman analysis. We fit the TDTR data with a model that accounts for pulse accumulation in a three layer system (90 nm Al, 275 nm SiO_2, and Si). We adjust h_K between the Al and the SiO_2 to determine the Al/SLG/SiO_2 thermal boundary conductance.

Figure 10 shows the thermal boundary conductance of the various graphene samples as a function of temperature. There is a clear increase in the overall h_K of the Al/SLG/SiO_2 contact for the O-functionalized graphene, yet a slight decrease in h_K for the H-functionalized graphene as compared to the reference sample. At room temperature, we show an increase in h_K of ~25% due to O-functionalization compared to the non-functionalized sample. As evident from the XPS and Raman analysis, both the H- and O-functionalization leads to increased sp^3 carbon bonds. In hydrogen, the C-H sp^3 bond is unreactive and thereby leaves the graphene surface inert.[101-103] However, it is well known that the addition of oxygen functional groups on a surface greatly changes the surface energy, leading to an enhanced adhesion at a metal/oxide interface. This is mainly due to the oxide's electronic and structural properties. It was shown for example, that graphene oxide has a higher surface energy compared to graphene.[104] Moreover, in the C-O bond, one electron from the oxygen molecule is shared with the carbon, which, in turn leaves an additional electron to bond with the metal surface, thereby increasing the bond strength between the Al and the graphene. We also note that both the H-SLG and O-SLG exhibit disorder as compared to the non-functionalized SLG (c.f. Fig. 9b). The effects of disorder on the cross plane thermal conductance of SLG are relatively minor and lead to a slight decrease, as determined by comparing the measured h_K at the Al/SLG/SiO_2 to the Al/H-SLG/SiO_2; we have previously observed similar reductions in h_K due to roughness at Al interfaces.[22] However, the functionalization process in this work does not lead to a significant increase in the surface roughness of the graphene films. Therefore, the enhancement in h_K is due to the enhanced bonding in the Al/O-SLG/SiO_2.

For comparison, we also show h_K measured at a SLG/SiO_2 interface[16] and a Al/graphite interface.[94] Using these values for h_K at the Al/graphite and SLG/SiO_2 interface, we can compare our measured conductance across the Al/SLG/SiO_2 interface to an empirical prediction based on the assumption that the overall interface conductance can be separated into two conductances in series on either side of the graphene, given by

$$h_{\mathrm{K,metal/SLG/SiO_2}} = \left(\frac{1}{h_{\mathrm{K,metal/SLG}}} + \frac{1}{h_{\mathrm{K,SLG/SiO_2}}} \right)^{-1}. \qquad (27)$$

This relation assumes that the cross plane thermal resistance of the SLG sheet is much less than the resistance at each of the interfaces, which is a valid assumption that has been addressed in detail previously.[18] Equation (27) is shown in Fig. 10 as the solid line, and shows relatively good agreement with our measured h_K across the Al/SLG/SiO_2 interface.

To directly compare the interface conductance between metals and SLG/graphite, we use Eq. (19) to estimate h_K across the metal/SLG interface by assuming that the SLG/SiO_2 thermal boundary conductance is the same as that measured by Chen *et al.*[16] and solving for $h_{\mathrm{K,metal/SLG}}$ for the Al/SLG and Al/O-SLG interfaces in this work. These values for h_K at the Al/SLG and Al/O-SLG interfaces are shown in Fig. 11 along with h_K across a Al/graphite interface[94] and across Al/diamond (Ref. 105) and Al/O-diamond (Ref. 106) interfaces. Our derived values for h_K at the Al/SLG interface are in very good agreement with the Al/graphite and Al/diamond data. We see a factor of two increase in h_K across the Al/O-SLG interface as compared with the Al/SLG data. This is consistent with the increase observed across the Al/O-diamond interface.

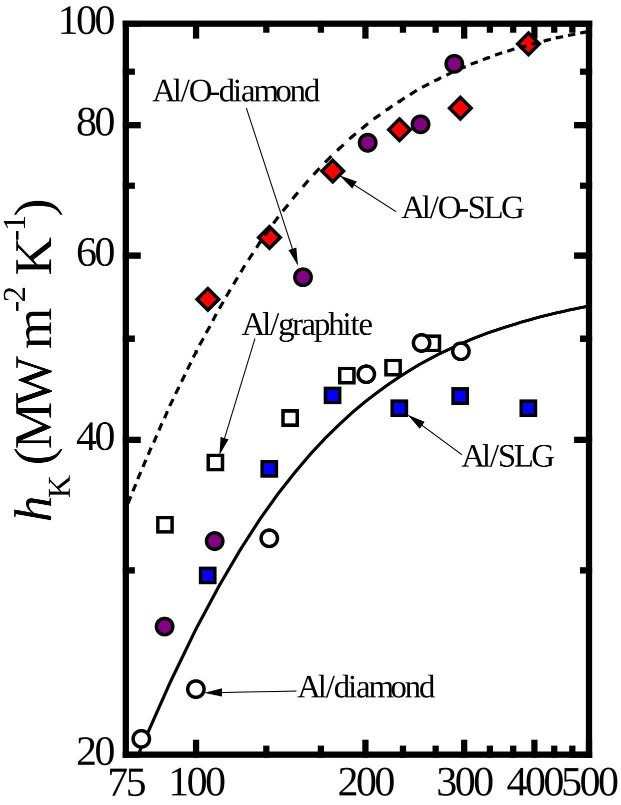

Fig. 11. Thermal boundary conductance across our Al/SLG (filled squares) and Al/O-SLG (filled diamonds) interfaces derived from our experimental measurements across the Al/SLG/SiO_2 and Al/O-SLG/SiO_2 interface along with Eq. (27) and the data from the SLG/SiO_2 interfaces.[16] The thermal transport across the Al/SLG interface increases by a factor of two with oxygen functionalization of the graphene. Our derived values for h_K across the Al/SLG interface are in good agreement with conductances measured across Al/graphite (open squares – Ref. 94) and Al/diamond interfaces (open circles – Ref. 105). Similarly, our derived values for Al/O-SLG h_K is in good agreement with Al/O-diamond measurements (filled circles – Ref. 106). We model the thermal conductance across the Al/SLG interface with the DMM, as shown by the solid line. We adjust the velocity of the SLG in our DMM calculations to model the Al/O-SLG thermal boundary conductance (dashed line), and find that the resultant velocity in the oxygenated SLG is about a factor of two higher than the non-functionalized sample. This is indicative of the increase in covalent bonds between the Al and the SLG via the oxygen adsorbates.

We attribute this increase to an increase in interfacial bonding between the Al and SLG or diamond. Recall that the presence of oxygen-containing functional groups increases the surface energy and thus makes it more reactive, allowing a lower energy bonding state with the evaporated Al film as compared to the untreated SLG or H-SLG, both of which are chemically inert.[101-103] This lower energy bonding state promotes Al-O formation, leading to a stronger Al-O-SLG junction and thereby an increase in h_K.

To quantify this, we turn to the diffuse mismatch model (DMM).[12] Assuming crystallographic isotropy in the Al film, the thermal boundary conductance from the Al to the SLG is given by Eq. (21). To calculate the transmission coefficient, we use the assumption discussed by Duda *et al.*[107] in which we treat the graphene sheet as a two dimensional solid. Therefore, performing detailed balance on the fluxes in the Al and SLG,[108] we obtain

$$\zeta_{1\to 2} = \frac{q_2}{q_1 + q_2}, \tag{28}$$

where q is the phonon flux. For the flux in the Al, we can make the usual approximation of phonon flux[2] given by Eq. (18). However, given the two dimensional nature of the SLG, the phonon flux in this material is given by[107]

$$q_2 = \frac{1}{8\pi a}\sum_j \int_{k_2} \hbar\omega_j(k) k f v_{2,j}(k) dk\,. \tag{29}$$

where a is the interlayer spacing of graphite (i.e., a = 3.35 Å).[109] For calculations for Al and graphene, we fit polynomials to the phonon dispersions of Al in the $\Gamma \to \mathrm{X}$ direction[75] and of graphene in the $\Gamma \to \mathrm{K}$ direction[110] to give greater accuracy in the DMM calculations as compared to the Debye approximation.[74] We note, however, that the modes in the $\Gamma \to \mathrm{K}$ in graphene are extremely Debye-like (i.e., non dispersive) in the frequency regime that is elastically accessible to the Al (frequencies below 10 THz). We ignore the ZA mode in the graphene dispersion since the ZA mode is heavily suppressed in encased and supported SLG.[89,111] We note that our calculations in Eq. (28) are balancing the total flux, and not the flux at any given frequency. We assume elastic scattering in this calculation. Therefore, we restrict the wavevector in each mode of the SLG and perform the integration only to the wavevector of the corresponding mode. As a result, no frequencies above the cutoff frequency of Al can participate in h_K. Also, given that our measurements represent the cross plane conductance of Al/SLG, the cross plane velocity of SLG is meaningless. Therefore, we define $v_{2,j}$ as a fitting parameter which we assume is constant with wavevector. This is a similar approach as performed in the analysis of Koh *et al.*[18] in which they adjust q_2 to fit the DMM to their Au/Ti/SLG data. We note that this approach of adjusting only $v_{2,j}$ gives us more direct insight into how the bonding at the Al/SLG interface changes due to the functionalization since we are not adjusting any aspect of the graphene dispersion, only the transport velocity. The fits of DMM are shown in Fig. 11. The solid line is the DMM calculation assuming that the graphene cross plane velocities are $v_{2,L} = 2{,}455\ \mathrm{m\,s^{-1}}$ and $v_{2,T} = 1{,}480\ \mathrm{m\,s^{-1}}$ for the longitudinal and transverse modes of the SLG, respectively. The dashed line is the DMM calculations assuming $v_{2,L} = 4{,}687\ \mathrm{m\,s^{-1}}$ and $v_{2,T} = 2{,}825\ \mathrm{m\,s^{-1}}$ for the longitudinal and transverse modes of the O-SLG, respectively. The velocities that result in the best fit of the DMM to the SLG data are in good agreement with the cross plane velocity of bulk graphite,[109] which could be indicative of similar bonding between the Al and SLG as the van der Waals bonds cross plane in graphite. The velocities resulting in the best fit in the Al/O-SLG data are nearly a factor of two higher, which we attribute to the increased bond strength between the Al and SLG due to the presence of oxygen leading to covalent bonding with the Al and O-SLG.

The data in Fig. 11 also give insight into the fundamental phonon mechanisms involved with thermal boundary conductance across Al and carbon-based materials. For example, Al/graphene, and Al/graphite, and Al/diamond all show similar values for thermal boundary conductance. However, these three carbon-based materials all have different dispersion relations, which by DMM considerations should result in different thermal boundary conductances. However, the DMM assumes a well bonded interface, and this could be indicative of the bonding at the Al/carbon-material interface being relatively weak compared to the bond strength in the Al and therefore not able to support all of the phonon frequencies in the thermal flux in the Al approaching the interface. This is further supported by the similar values in h_K that we observe

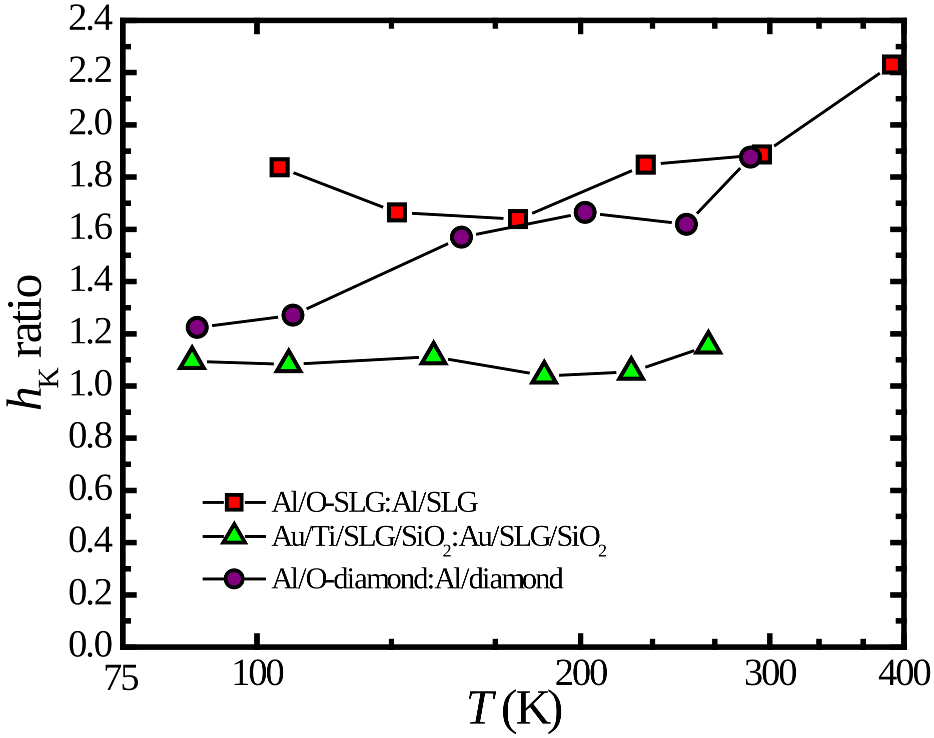

Fig. 12. Ratio of thermal boundary conductance Al/O-SLG to Al/SLG (filled squares). For comparison, we also plot the ratio of h_K across the Al/O-diamond interface[106] to the Al/diamond interface[105] (filled circles). These ratios are very similar, especially at elevated temperatures, which would be indicative of a similar increase in the elastic constants at the Al-O bond compared to the Al-graphene or Al-diamond bond. We plot the ratio of h_K across a Au/(2nm)Ti/SLG/SiO$_2$ interface[5] to h_K across an Au/graphite interface[94] (filled triangles). The two conductances are nearly identical over the entire temperature range (i.e., Au/(2nm)Ti/SLG:Au/graphite ~ 1). Where the Ti will increase the bond strength, Au is a very soft material with low phonon velocities and weak elastic constants. Therefore, the phonon flux in gold is so low that regardless of the strength of the bond at the Au/SLG or graphite interfaces, the phonon transmissivity will always be limited by the phonon flux in the Au.

when we functionalize graphene with oxygen compared to the oxygen terminated diamond studied by Collins *et al*.[106] For comparison, we plot the ratio of our Al/O-SLG data to our Al/SLG data (Al/O-SLG:Al/SLG) along with the ratio the Al/O-diamond to Al/diamond (Al/O-diamond:Al/diamond), shown in Fig. 12. These ratios are very similar, especially at elevated temperatures, which would be indicative of a similar increase in the elastic constants at the Al-O bond compared to the Al-graphene or Al-diamond bond. Also in this figure, we plot the ratio of h_K across a Au/(2nm)Ti/SLG/SiO$_2$ interface [5] to h_K across an Au/graphite interface.[94] Presumably, the Ti wetting layer between the Au and SLG should increase the wettability of the Au to the SLG. However, the two conductances are nearly identical over the entire temperature range (i.e., Au/(2nm)Ti/SLG:Au/graphite ~ 1). Where the Ti will increase the bond strength, Au is a very soft material with low phonon velocities and weak elastic constants. This corresponds to a low thermal flux of phonons approaching the interface. Therefore, the phonon flux in gold is so low that regardless of the strength of the bond at the Au/SLG or graphite interfaces, the phonon transmissivity will always be limited by the phonon flux in the Au; this is further supported by the fact that the phonon velocities in Au are very similar to the cross plane velocities of graphite. This interplay between the phonon flux that is supported in a given material and the bond strength at the material/SLG interface has major implications for engineering and development of graphene-based devices in which contact resistances plague the device performance.

In summary, we have investigated the effects of molecular functionalization, and subsequent bonding, has on the thermal boundary conductance across metal/graphene interfaces. We pursued this by introducing chemical adsorbates on the SLG surfaces in order to increase the density of covalent bonds bridging the metal and the SLG. Specifically, we metalized plasma functionalized graphene and then measure h_K at Al/SLG/SiO$_2$ contacts with time domain thermoreflectance techniques. Through these measurements, adsorbates on the SLG surfaces were shown to influence the cross plane thermal conductance. These influences are attributed to changes in the bonding between the metal and the SLG that itself is affected by increased disorder within the SLG. The thermal boundary conductance was found to be most influenced by the interfacial chemical bonding as both the phonon flux and the vibrational mismatch between the materials are each subject to the interfacial bond strength. Through these experimental results, we also demonstrated plasma-based funtionalization of graphene surfaces as a means to manipulate the thermal boundary conductance.

4.3. Tunable, ultra-low thermal conductivity of nanoparticle films (Hopkins, Mittal, Phinney, Grillet, and Furst, *Applied Physics Letters* 99, 133106 (2011)).

As discussed in Section 4.1, the ability to control the thermal transport in materials is a fundamental goal in the development and thermal management of nanosystems. As we have seen throughout the last two sections, controllable reduction in the thermal conductivity of nanosystems arise from tailoring structure in interface densities (i.e., manipulating the thermal boundary conductance). However, this subsequent decrease in thermal conductivity from interface engineering often comes at a cost. For example, fabrication and construction of nanoparticle composite films with large interface densities can prove intricate and costly, thereby proving difficult to reap the benefit of the unique thermal properties for larger area thermal insulation applications. In addition, increasing the density of nanoparticles in a composite material will also adversely affect the electrical conductivity due to increased electron scattering events, thereby decreasing the thermoelectric efficiency. Therefore, an efficient, controlled, and scalable methodology of creating a class of nanomaterials with variable thermal properties is immensely important to further the progress of low thermal conductivity material systems.

In addition to the end goal of reducing the thermal conductivity of nanoparticle systems, controlled fabrication techniques also offer the unique opportunity to study the phonon scattering mechanisms involved in thermal transport in nanoparticle-laden structures. A recent theoretical study[57] predicted that spherical, cubically-packed nanoparticles will have thermal conductivities below the minimum limit[112] due to a large resistance from interfacial scattering between the nanoparticles. Presumably, with controlled nanoparticle arrangements, the frequency of the interfacial scattering events can be tuned, thereby introducing new avenues for manipulation of thermal transport, which has far reaching implications for next-generation applications involving solid-state thermal rectification[113,114] and asymmetric heat conduction[115,116] such as the design of a thermal transistor[117] or a thermal storage device.[118]

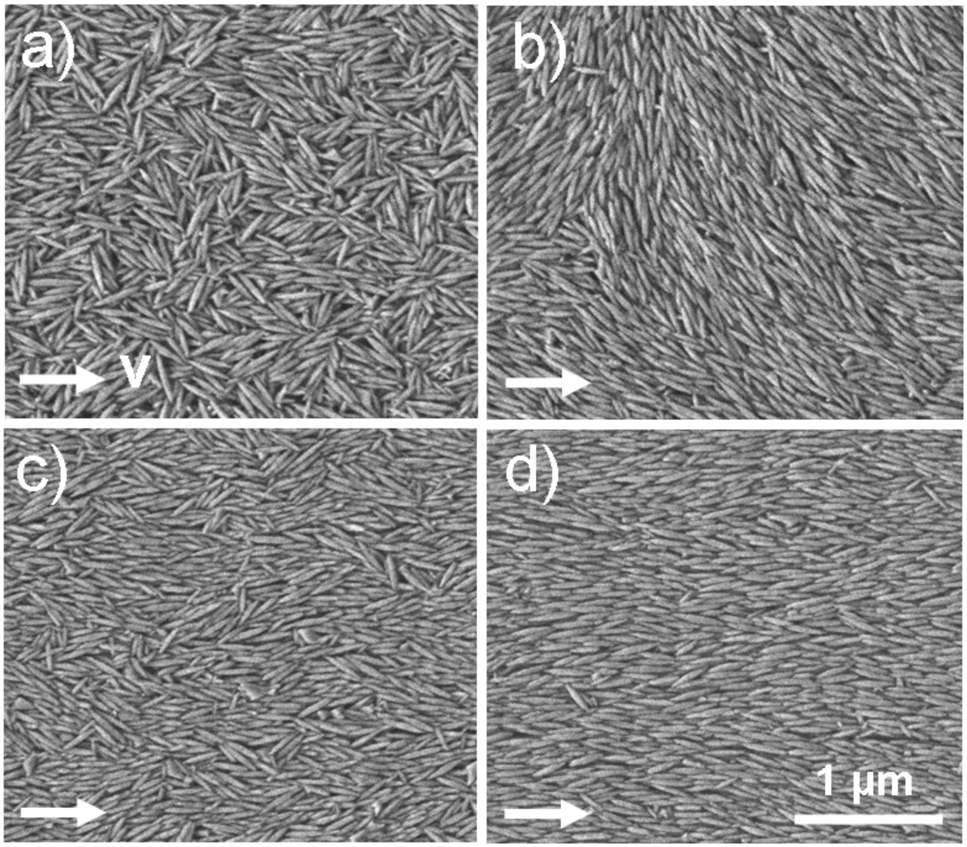

Fig. 13. SEM images of the deposited films. (a) $\phi = 0.24$, $v = 125$ μm/s, P_2 = 0.335 (b) $\phi = 0.24$, $v = 1500$ μm/s, P_2 = 0.185 (c) $\phi = 0.52$, $v = 125$ μm/s, P_2 = 0.730 (d) $\phi = 0.52$, $v = 1500$ μm/s, P_2 = 0.885. The arrow denotes the coating direction. The scalebar is 1 μm.

In this work, we measure the thermal conductivity of a series close-packed nanoparticle films with time domain thermoreflectance (TDTR).[26,44,119] The films are fabricated on aluminum coated glass substrates by flow coating a suspension of ellipsoidal colloidal titantia nanoparticles, resulting in structured films with tailored order. The thermal conductivities of these nanoparticle films are nearly an order of magnitude less than that of polycrystalline TiO_2 films with similar grain sizes. The thermal conductivities are dependent on nanoparticle orientational order, and films with more randomly oriented particles exhibit thermal conductivities less than the amorphous limit. The temperature trends in the thermal conductivities suggest that, in addition to Umklapp and grain boundary scattering in the TiO_2 nanoparticles, thermal boundary resistance between individual nanoparticles is contributing to the ultra-low thermal conductivity of these convectively assembled TiO_2 nanoparticle thin films.

Ellipsoidal titania particles are synthesized by a “gel-sol” chemistry in the presence of ethylenediamine.[120] The polycrystalline nanoparticles have an equatorial radius $a = 24 \pm 4$ nm, a polar radius $b = 130 \pm 31$ nm and a density of 2.74 ± 0.10 g/cm^3. Films of titania particles are deposited on aluminum coated glass slide by flow coating.[121,122] Briefly, a stable colloidal suspension of the titania nanoparticles suspended in ultra-pure water (resistivity$\geq$18.2 MΩ· cm) is confined between the substrate and a glass blade positioned 200 μm above and at 25° inclination. The nanoparticle volume fractions in the suspensions prior to coating, ϕ, are below ($\phi = 0.24$) and above ($\phi = 0.52$) the isotropic-nematic transition, $\phi^* \approx 0.4$. The substrate is

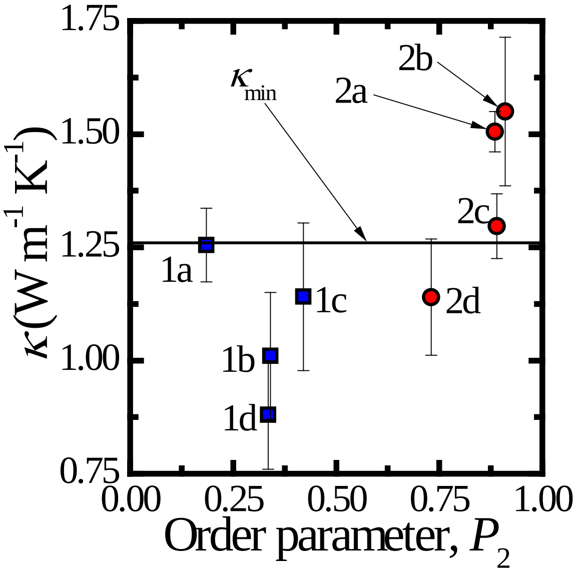

Fig. 14. The thermal conductivity of the films (κ) measured at the room temperature as a function of order parameter (P_2), estimated from SEM images via Eq. (29). The minimum thermal conductivity of TiO_2 is also shown (κ_{min} – Eq. (31)). The orientational ordering, which is controllable during the assembly process, can be used to tune the thermal conductivity across the theoretical minimum limit.

translated by a computer controlled motorized stage at a velocity, v of (a) 125 μm/s, (b) 1500 μm/s, (c) 125 μm/s and (d) 1500 μm/s. Prior to coating, the substrate is washed thoroughly with ultra-pure water, followed by plasma cleaning (Model PDC-32G, Harrick Plasma). The film structure depends on both the nanoparticle loading and the substrate velocity during the coating. A detailed description of the effect of experimental parameters on the film structure is described elsewhere.[122] Scanning electron microscopy (SEM) images in Fig. 13 show the film structures for samples used in this study. The nanoparticles in the films exhibit different ordering parameters, as discussed in more detail in the supporting information. At $\phi = 0.24$ and $v = 125\,\mu\mathrm{m/s}$ (Fig. 13a), the particles are deposited with random alignment. Increasing the substrate velocity introduces domains of similar nanoparticle alignment and subsequently leads to increases in the size of these domains, as seen for $\phi = 0.24$ and $v = 1500\,\mu\mathrm{m/s}$ (Fig. 13b – although these domains are not aligned with the coating direction). At $\phi = 0.52$ nanoparticles are oriented on average along the coating direction, with the alignment increasing as the substrate velocity is increased from $v = 125\,\mu\mathrm{m/s}$ (Fig. 13c) to $v = 1500\,\mu\mathrm{m/s}$ (Fig 13d). We characterize the orientational order of the nanoparticles in each film by image analysis using the order parameter

$$P_2 = \sum_{i=1}^{N} \cos(2\theta_i) \Big/ N\,, \tag{29}$$

where θ_i is the angle of particle i relative to the flow coating direction and N is the number of particles in each image. Varying the substrate velocity and the particle volume fraction also changes the thickness of the deposited film.

We measured the thermal conductivity of the thin films of convectively assembled TiO_2 nanoparticles with TDTR[26,44,119] in a "probe through the glass" geometry that we discuss

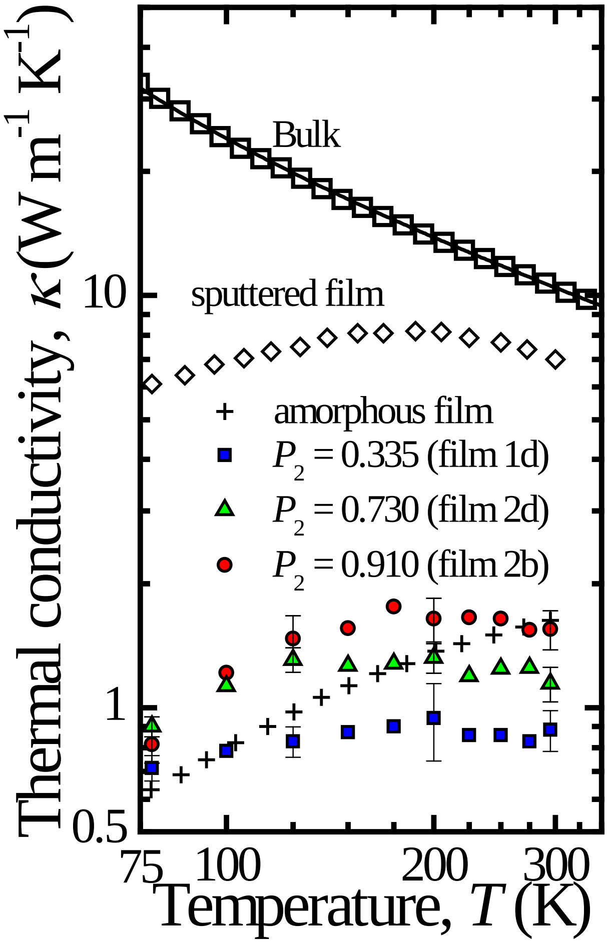

Fig. 15. Thermal conductivities of three different films – an ordered film (2b), a disordered film (1d), and a moderately ordered/disordered film (2d). Representative error bars are shown which represent the standard deviation calculated from the 5 different measurements on each sample. For comparison, we also plot the thermal conductivity of bulk, single crystalline TiO_2 (Ref. 124), a polycrystalline sputtered film with ~17 nm grain size,[125] and an amorphous TiO_2 film.[126] The thermal conductivity of the nanoparticle based films nearly an order of magnitude lower than the sputtered TiO_2 film with similar grain sizes. The measured thermal conductivities of the nanoparticle films have similar values of κ as the amorphous film but temperature trends similar to the polycrystalline sputtered film indicating that the phonon transport in the nanoparticle films is not limited by the interatomic spacing or lack of periodicity as in the amorphous film. This implies that three-phonon scattering and boundary scattering are still dominant phonon scattering events in these nanoparticle films with extremely low thermal conductivity.

elsewhere.[123] We note that this geometry requires different thermal modeling than discussed in Section 3, as we discuss in detail in Ref. 123. The room temperature thermal conductivities of the eight different films as a function of order parameter are shown in Fig. 14. There is a clear trend between the order parameter of the samples and the thermal conductivity, indicating that there is some level of tunability between the thermal transport in the film and the orientation of the nanoparticles.

To examine the temperature trend in κ of the TiO_2 films, we measure the thermal properties of three different films – an ordered film (2b), a disordered film (1d), and a moderately ordered/disordered film (2d) – over the range from 77 – 300 K by mounting the samples in a LN_2 controlled cryostat with optical access pumped down to pressures less than 1.0 mTorr. The average thermal conductivities of three films as a function of temperature are shown in Fig. 15. Representative error bars are shown which represent the standard deviation calculated from the 5 different measurements on each sample. For comparison, we also plot the thermal conductivity of bulk, single crystalline TiO_2 (Ref. 124), a polycrystalline sputtered film with ~17 nm grain size,[125] and an amorphous TiO_2 film.[126] We estimate the grain sizes of the TiO_2 nanoparticles from high resolution TEM images as ~15 nm. The thermal conductivity of the nanoparticle based films in this study are significantly lower, nearly an order of magnitude in some cases, than the sputtered TiO_2 film with similar grain sizes. The measured thermal conductivities of the nanoparticle films have similar magnitudes of κ as the amorphous film but temperature trends similar to the polycrystalline sputtered film indicating that the phonon transport in the nanoparticle films is not limited by the interatomic spacing or lack of periodicity as in the amorphous film. This implies that three-phonon scattering and boundary scattering are still dominant phonon scattering events in these nanoparticle films with extremely low thermal conductivity.

To investigate the thermal conductivities of these TiO_2 close-packed nanoparticle films, we model the thermal conductivity in TiO_2 with an approach similar to that outlined by Callaway[127] and Holland.[128] In short, we treat the TiO_2 samples as isotropic Debye media and model the thermal conductivity with

$$\kappa_p = \frac{1}{3}\sum_j \int_\omega C_j(\omega) v_j^2 \tau_j(\omega) d\omega, \qquad (30)$$

where C_j is the specific heat per normal mode at frequency ω and τ_j is the scattering time and the summation is over j = 3 polarizations (1 longitudinal and 2 degenerate transverse). Under the Debye treatment, the heat capacity is $C_j = \hbar\omega^3 (\partial n/\partial T)/(2\pi^2 v_j^3)$ where $\hbar$ is the reduced Planck's constant, n is the Bose Einstein distribution, and T is the temperature. For a TiO_2 Debye crystal, we assume that the longitudinal and transverse phonon velocities are 9,200 and 5,100 m s^{-1}, respectively[125] (note that this approach of modeling the thermal conductivity of bulk TiO_2 under the Debye approximation with longitudinal and transverse modes was also successfully employed by Lee *et al.*[125]). In a treatment similar to that outlined by Mingo,[129] we fit Eq. (30) to the thermal conductivity of bulk TiO_2 to determine the intrinsic three-phonon and impurity scattering times. Taking the form of the scattering times as $\tau_{3,j} = (AT\omega^2 \exp[-B/T])^{-1}$ for three-phonon and $\tau_{I,j} = (D\omega^4)^{-1}$ for impurity, the coefficients A, B, and C are used as fitting parameters to fit Eq. (30) to the thermal conductivity data of bulk TiO_2. The best fit is shown as the black line through the bulk TiO_2 data in Fig. 15. This was achieved with $A = 6.4\text{x}10^{-19}$ s K^{-1}, B = 82 K, and $D = 1.7\text{x}10^{-42}$ s^3.

Where Eq. (30) gives the thermal conductivity of single crystalline TiO_2, the opposite extreme of TiO_2 transport is given by the minimum limit to thermal conductivity. This limit, originally proposed by Einstein[130] restricts the phonon mean free path to the interatomic spacing. Cahill *et al.*[112,131,132] later revised this limit to account for a Debye solid. In the Cahill limit, $\tau = \pi/\omega$, and assuming a Debye dispersion, the thermal conductivity is given by

$$\kappa_{\min} = \frac{1}{6\pi}\sum_j \frac{1}{v_j}\int_\omega \hbar\omega^2 \frac{\partial n}{\partial T} d\omega. \qquad (31)$$

To understand the phonon scattering mechanisms contributing to the observed thermal conductivities in the nanoparticle films, we model the thermal conductivity in an individual nanoparticle with Eq. (30) using the three-phonon and impurity scattering times determined from the bulk fit and incorporate an additional grain boundary scattering time given by $\tau_{g,j} = d/v_j$, where we approximate d in the nanoparticles as 15 nm from high resolution TEM of the nanoparticles, as previously mentioned. This approach, while accounting for phonon scattering mechanisms in the nanoparticle, does not explain the different observed κ in the "ordered" (film 2b) and "disordered" (film 1d) films. To explain this, we consider the effect of thermal boundary resistance, R_K, between the nanoparticles by taking the overall thermal conductivity of the nanoparticle film as[133]

$$\kappa = \frac{\kappa_p}{1 + \frac{R\kappa_p}{d}}, \tag{32}$$

where d is the characteristic distance that the phonons traverse in the nanoparticle before scattering at the nanoparticle-nanoparticle interface and κ_p is calculated from Eq. (30). We estimate the thermal boundary resistance as 2.0×10^{-8} W^{-1} m^2 K, an average value for resistances involving oxides,[48,133] and consider two limiting cases of phonons propagating the length (260 nm) or width (48 nm) of the nanoparticle before experiencing an interfacial scattering event. As seen in Fig. 16, the model accounting for "most-ordered" (2b) and "most-disordered" (1d) films describes the measured data remarkably well. For comparison, we also show the theoretical minimum thermal conductivity of TiO_2.[112,130,134] The theoretical minimum thermal conductivity does not capture the temperature trends in the nanoparticle packed films. The temperature trends of the nanoparticle films, which are indicative of a polycrystalline material, indicate that three-phonon scattering events are still playing a role in the thermal transport in the nanoparticle films. The magnitude of the thermal conductivity is lowered from particle-particle interface scattering, with this scattering rate increasing with nanoparticle disorder. In the heavily disordered case, the thermal conductivity is less than the theoretical minimum limit. The thermal conductivity of the polycrystalline nanoparticle film is tunable by controlling the nanoparticle ordering and thereby controlling the frequency of the nanoparticle interfacial scattering events, or the interparticle thermal boundary resistance. This is not possible in amorphous films where phonons can be scattered at a distance of the interatomic spacing, as described by the minimum limit. However, in the polycrystalline nanoparticle films, phonons that propagate the size of the nanoparticle are scattered at the nanoparticle interfaces, giving the tunability to thermal conductivity based on the frequency of the inter-nanoparticle scattering events. This aspect of nanoparticle orientation that is controllable during assembly can be used to tune the thermal conductivity of the nanoparticle packed film across the theoretical minimum limit (see Fig. 14).

In summary, we report on the ultra-low thermal conductivity of a series of convectively assembled, anisotropic titania (TiO_2) nanoparticle films. The TiO_2 films are fabricated on aluminum coated glass substrates by flow coating a suspension of ellipsoidal colloidal nanoparticles, resulting in structured films with tailored order. Time domain thermoreflectance is used to measure the thermal conductivity of the TiO_2 films. The thermal conductivities of these nanoparticle films are nearly an order of magnitude less than that of polycrystalline TiO_2 films with similar grain sizes. The thermal conductivities are dependent on nanoparticle orientational order and films with more randomly oriented particles exhibit thermal conductivities less than the amorphous limit. The temperature trends in the thermal

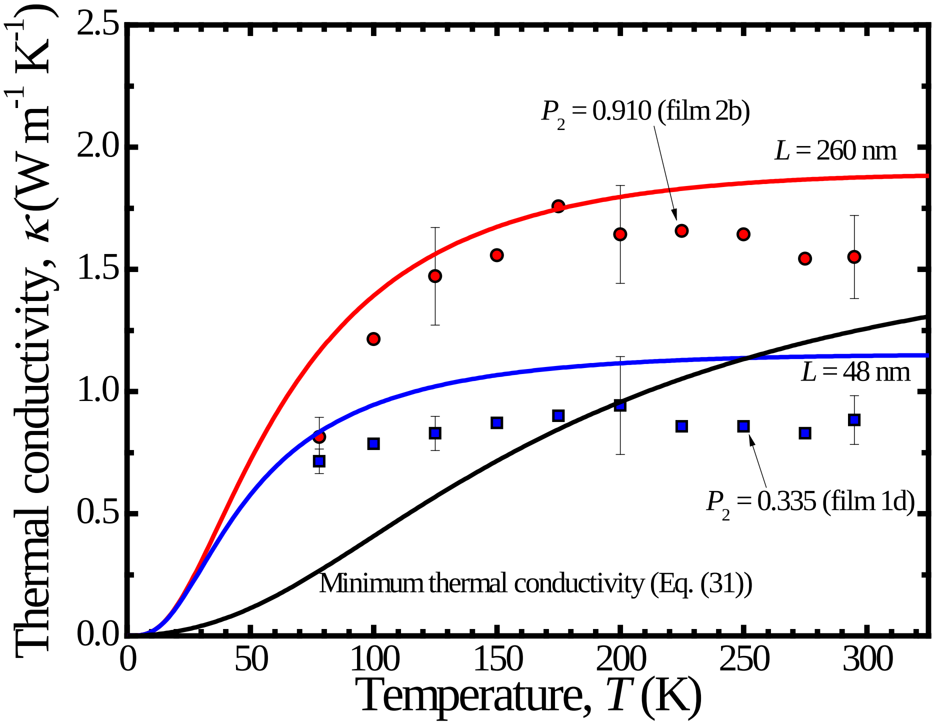

Fig. 16. Thermal conductivity of film 2b (ordered) and film 1d (disordered) as a function of temperature. The temperature trends of the experimental data are different than those predicted by the minimum limit. We model the thermal conductivity of the films by considering Umklapp, impurity and grain boundary scattering and interparticle thermal boundary resistance. *d* = 260 nm and *d* = 48 nm correspond to the length and width of a TiO_2 nanoparticle, respectively, and are the bounds on the distance a phonon can propagate before scattering.

conductivities suggest that, in addition to Umklapp and grain boundary scattering in the TiO_2 nanoparticles, thermal boundary resistance between individual nanoparticles is contributing to the ultra-low thermal conductivity of these convectively assembled TiO_2 nanoparticle thin films. The tunablility of the thermal conductivity is driven by the nanoparticle ordering and thereby controlling the frequency of the nanoparticle interfacial scattering events. This nanoparticle ordering presents a unique method to tune the thermal conductivity of nanocomposites to ultra-low values below the theoretical minimum limit.

4.4. Minimum thermal conductivity considerations in aerogel thin films (Hopkins, Kaehr, Piekos, Dunphy, and Brinker, *currently under review*).

As discussed in the previous three subsections, the promise of materials in which the electrical, thermal and mass transport properties are "user-defined" with nano-scale precision has fueled an enormous thrust in the materials science community to develop nanomaterials and fabrication strategies.[3,135] The development of approaches to control nano-structure morphology using self-assembly has drastically simplified nanomaterial synthesis, enabling rapid, low-temperature processing of thin films for use as membranes, dielectric insulator layers, and optical coatings.[136]

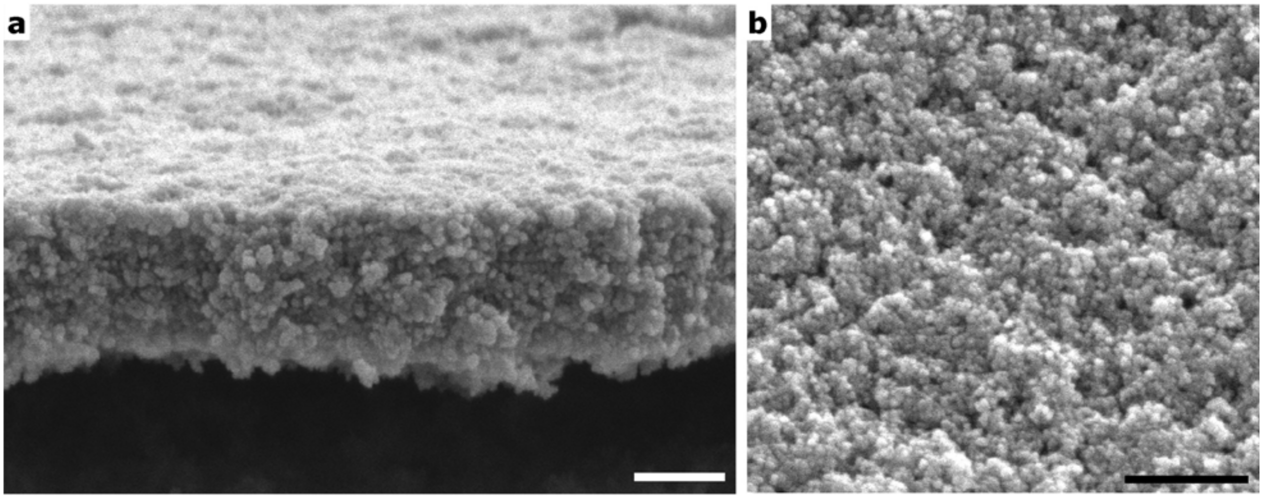

Fig. 17. Scanning electron microsocpy image of the (a) cross section and (b) top view of a thin film aerogel. The scale bars are 500 nm.

Despite these advances in thin film processing, characterization of the physical properties in nano-structured thin films remains a considerable challenge due to complex geometries and non-conformal surface areas. For example, measuring heat transport in highly thermally insulating materials such as aerogels, let alone aerogel thin films, has proven to be particularly challenging using standard approaches due to convective and radiative losses.[137-140] Understanding heat transport in thin porous films is critical for low-k dielectric applications in microelectronics as well as optical coatings for solar panels.[44] In this work, we overcome these challenges and demonstrate the use time domain thermoreflectance (TDTR) to measure the thermal conductivity of aerogel thin-films from 80 – 294 K. We adopt the "probe through the glass" the test geometry, as discussed in Section 4.3. We theoretically describe the thermal transport in the aerogel films with a modified minimum limit to thermal conductivity that accounts for porosity through a reduction in phonon velocity. We find that our porous minimum limit agrees well with a wide range of experimental data.

To prepare the aerogel samples, we evaporate 85 nm of Al on VWR micro cover glass (No. 48368040). We then fabricate the aerogel thin films on the surface of the Al film. The thin aerogel films were prepared using identical procedures as previously described.[141] Briefly, silica sols were prepared from a stock solution (tetraethoxysilane, EtOH, H20, HCl in a $1.0:3.8:1.1:7.0\text{x}10^{-4}$ molar ratio), refluxed (60°C, 90 min) and gelled at 50°C. Surface hydroxyls were partially replaced with methyl groups using hexamethyldisilazane (HMDS) as the derivatizing agent and sonicated to reliquify the solution. The solution was spin coated (2000 rpm, 30 sec) onto the Al coated glass. During evaporation the film gels, shrinks due to drying stresses, and springs back to create a high porosity aerogel film. We refer to these films as "aerogel". After initial TDTR measurements, the aerogel films were calcined (500°C, 3 hrs) to remove the methyl groups. We refer to these films as "calcined-aerogel". We also perform TDTR measurements on Al coated glass with no silica film as a calibration. This allows us to accurately determine the thermal conductivity of the cover glass and the thermal boundary conductance between the Al film and cover glass, thereby reducing the number of free parameters in the thermal model needed to determine the thermal conductivity of the aerogel samples. Scanning electron microscopy images of a thin film aerogel are shown in Fig. 17.

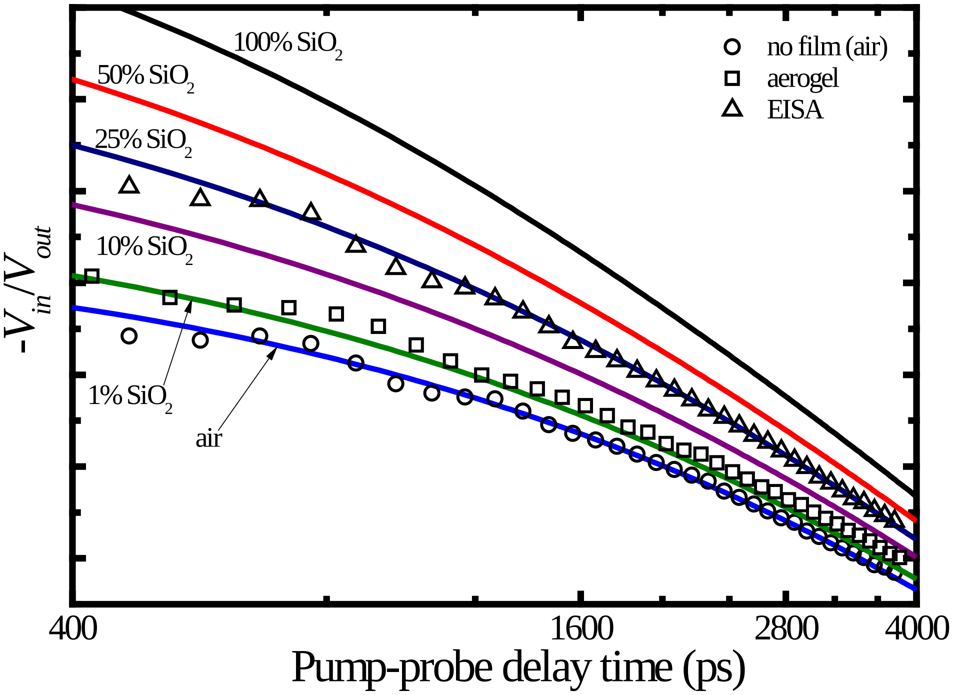

Fig. 18. TDTR data from the EISA and aerogel films along with data from the sample with no film (i.e., air). The solid lines represent the predictions from the thermal model for various reductions in the SiO_2 sample thermal conductivity.

Figure 18 shows sample TDTR data of the aerogel films along with data from the sample with no film (i.e., air) and data from a previously examined mesoporous silica film (``EISA").[123] Along with the data, we show the predictions from the thermal model for various reductions in SiO_2 sample κ. Since the pump is modulated at 11 MHz, the TDTR data represent measurements of the thermal effusivity of the porous SiO_2 sample, $E = \sqrt{C\kappa}$.[47] We fit the data from the sample with no SiO_2 or aerogel film by adjusting the value for the h_K between the glass slide and the Al film and κ for the glass slide. Due to the low thermal conductivity of the aerogel samples, the TDTR signal is relatively insensitive to the Al/sample thermal boundary conductance.[123,142] The presence of any thermal mass on the free surface of the Al increases the TDTR signal. In fact, TDTR has the sensitivity to be able to measure thermal conductivities of samples with thermal effusivities in the solid matrix of the porous sample as low as 10% of bulk SiO_2, representing a reduction in thermal conductivity to 1% of bulk.

The model calculations and subsequent data analysis in this work (and shown in Fig. 18) require inputs of both κ and C for each layer and h_K for interfaces. As we have previously discussed our determination of the various values for κ and h_K, we focus now on our assumptions of heat capacity, C, in each layer, notable, the assumption of heat capacity for highly porous films during TDTR. For both the glass slide and Al film, we assume a bulk heat capacity, which is typical in TDTR experiments for metal transducers and semi-infinite, bulk substrates. We can also assume that the solid portion of the aerogel film has a heat capacity equivalent to bulk SiO_2 which is valid at temperatures above ~20 K.[143] In TDTR, all the thermal energy is absorbed in the Al transducer and then partially transmitted into the aerogel and glass. We then monitor the thermal decay in the Al film over ~ 4 ns. This 4 ns of decay is not enough time for any of the thermal energy to conduct into the air from the silica ligaments in the aerogel. This means that the only media that our measurement detects are the silica ligaments in the aerogel. Therefore, the thermal decay in any porous film (i.e., aerogel) in TDTR is related to the reduced thermal conductivity in the solid ligaments and the bulk heat capacity of the material comprising the ligaments.

This assumption, which demonstrates a very powerful aspect of TDTR for easily determining the thermal conductivity of porous materials, must be justified further. To ensure that there is no conduction from the aerogel films to the air, we test the samples in ambient and under vacuum at room temperature. We find no change in the measured TDTR signal and subsequent effusivity in any of the samples. This indicates that the air in the pores is not contributing to the thermal effusivity in the time domain of the measurement. Our vacuum pumps the cryostat chamber down to less than 1.0 mTorr, which is sufficient pressure to remove any contribution we would have observed from conduction through the air in the aerogel samples.[139] Given this observation, we can now theoretically analyze the heat flow in the porous sample (i.e., aerogel film) during TDTR via the ``two-fluid" model for heat transfer in porous media.[144] In the most general of experiments in which energy is absorbed in both the solid (silica) and fluid (air) phases, and the two phases are not in equilibrium, the heat conduction is governed by

$$(1-\Phi)C_s \frac{\partial T_s}{\partial t} = (1-\Phi)\kappa_s \nabla^2 T_s - h\left(T_s - T_f\right) + (1-\Phi)P\,, \tag{33}$$

for the solid phase and

$$\Phi C_f \frac{\partial T_f}{\partial t} = \Phi \kappa_f \nabla^2 T_s + h\left(T_s - T_f\right) + \Phi P\,, \tag{34}$$

for the fluid phase, where Φ is the porosity of the medium, defined as the volume fraction of the fluid (air), h is the heat transfer coefficient between the solid and fluid, P is the volumetric absorbed power, and the subscripts s and f refer to the solid (silica) and fluid (air), respectively. Since there is no conduction from the aerogel to the air during our TDTR experiments, $h = 0$. Because of this, we can also assume that all the heat absorbed in the Al transducer film is transferred to the slica solid, and not to the air, so that $\Phi P = 0$. Given that there is no heat transferred to the fluid (air) during the time domain in TDTR, there is no temperature gradient and therefore no heat transfer in the fluid (air). This means that the transient conduction in the porous film is governed solely by the heat transfer in the solid matrix. Furthermore, since all the heat is absorbed by the solid, the fractional porosity factor 1-Φ cancels out of Eq. (33), and the heat capacity governing the transient decay during TDTR is simply the bulk heat capacity of the solid ligaments. This demonstrates the convenience for using TDTR to measure thermal conductivity of porous material; that is, over the time domain interrogated in TDTR measurements (a few nanoseconds), we only observe thermal conduction through the solid matrix of the samples and do not observe any aspect of the air or gas in the porous material. We validated this assumption via experiments under evacuated and ambient conditions, as previously discussed. This is further supported by comparing the thermal effusivity of silica to that of air ($E_{\text{air}}/E_{\text{silica}} \sim 0.004$) which indicates that there is a negligible amount of heat transferring into the air compared to the silica. Note that this same measurement convenience is applicable to all porous materials assuming there is not heat transfer from the solid to the air.

We plot the thermal conductivity of the samples as a function of measured SiO_2 atomic density, n_p, for the EISA, aerogel, and calcined-aerogel films in Fig. 19 along with the thermal conductivity of bulk SiO_2,[49] a sputtered SiO_2 thin film,[13] other porous silica materials (XLK and FOx),[40] and bulk SiO_2 aerogels.[139,145] The error bars in our measurements represent the standard

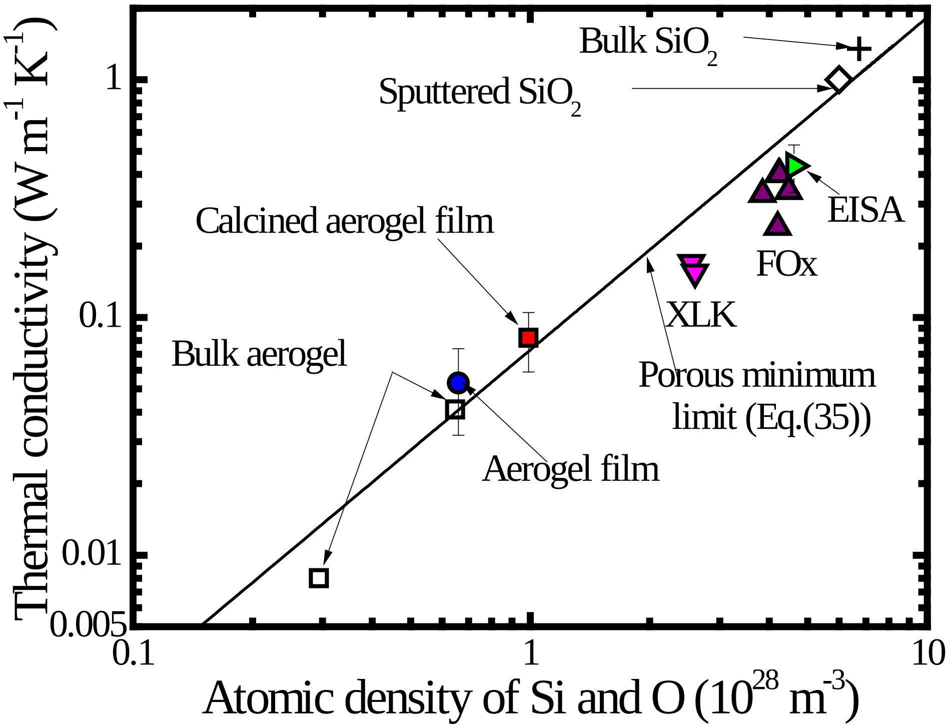

Fig. 19. Thermal conductivity as a function of volumetric atomic number density of silicon and oxygen for the EISA, aerogel, and calcined-aerogel films along with bulk SiO_2,[49] a sputtered SiO_2 thin film,[13] and bulk SiO_2 aerogels.[139,145] Predictions from the theoretical "porous minimum limit" to the thermal conductivity of SiO_2 (solid line - Eq. (35)) that is derived in this work shows good agreement with the thermal conductivity of the porous silica structures.

deviation about the mean value of κ determined from multiple data sets taken on each sample type (upwards of 10 different TDTR scans taken on each sample and two samples of each type of silica film). We measure the SiO_2 compositional percentage[146] and sample porosity in the EISA and aerogel films using ellipsometry and surface acoustic wave techniques.[147] We note that burning off the methyl groups from the aerogel skeleton increases the density and thermal conductivity of the film. This is most likely a consequence of silica condensation following exposure to air of free silanol groups which may lead to increased silica network connectivity. In Fig. 19, we compare our data to thermal measurements on silica materials that do not include opacifiers such as carbon soot (thus excluding the data reported in Refs. 138 and 140).

In amorphous materials such as silica glass, thermal transport is limited by atomic scattering at a distance of the interatomic spacing.[130] This lower limit to thermal conductivity is described by the theoretical minimum thermal conductivity in which the ``phonon" scattering rate is wavelength limited, as discussed in Section 4.3. This minimum limit is given in Eq. (31). We plot Eq. (31) as a function of atomic density in Fig. 20, assuming the longitudinal and transverse sound velocities of SiO_2 are 5,800 and 3,700 m s^{-1}, respectively, and $n_{bulk} = 6.74 \times 10^{28}$ m^{-3}.[49,79]

The major assumption in applying Eq. (31) to describe thermal conductivity as a function of SiO_2 atomic density is that the sound velocity can still be described by the bulk velocities in SiO_2. This clearly is not a valid assumption throughout the entire structure due to the porosity, and resulting matrix of overlapping and multidirectional solid ligaments that cause a reduction in sound velocity.[40] To address this in the minimum model, we modify the group velocity to scale

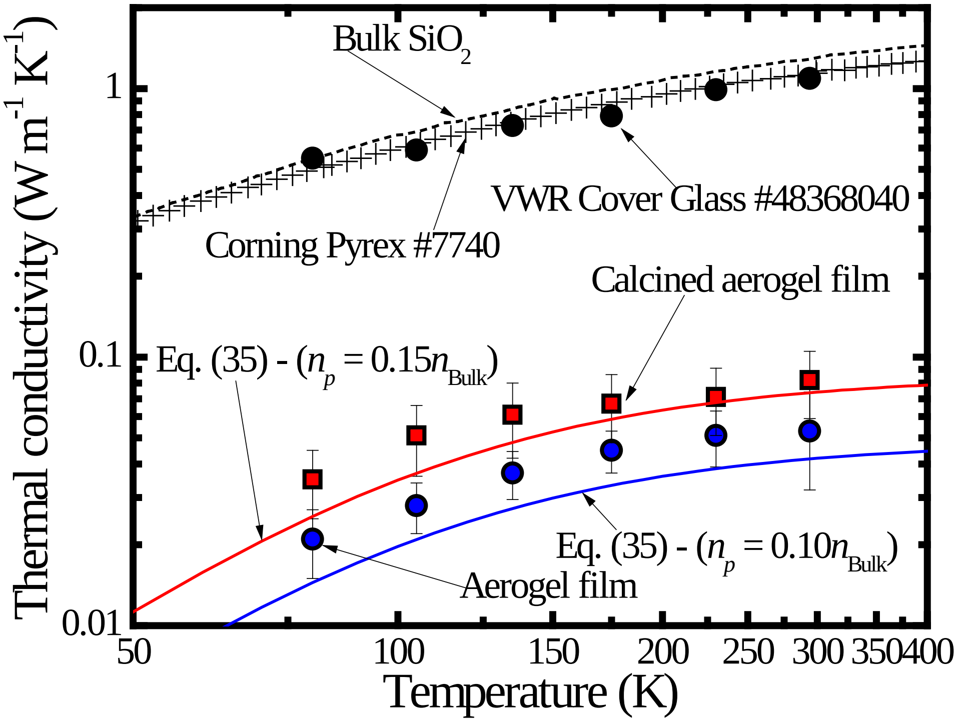

Fig. 20. Thermal conductivity cover glass substrate and the two aerogel films from this work as a function of temperature. We plot our "porous minimum limit" that is given in Eq. (35). Our "porous minimum limit" agrees well with our measured κ on the aerogel films well. We also show the measured thermal conductivity of our cover glass (VWR Cover Glass #48368040) with previously measured values of Corning Pyrex #7740 and bulk SiO$_2$ for comparison.[20,49]

with the number density in the overall volume of the sample. Note that, as we have previously discussed, we assume that the heat capacity of the solid ligaments in the aerogel can be described as bulk. Therefore, the phase velocities and cutoff frequencies must remain unchanged in our model to predict the thermal conductivity of porous silica, and only the group velocities that represent the velocity of thermal transport must be scaled. The group velocities in porous silica structures scale by $(n_p/n_{\mathrm{bulk}})^{1.4}$ (Ref. 40). Therefore, Eq. (31) can be recast as a "porous minimum limit" given by

$$\kappa_{\min} = \frac{1}{6\pi}\sum_j \frac{1}{v_j}\int_\omega \hbar\omega^2 \left(\frac{n_p}{n_{\mathrm{bulk}}}\right)^{1.4} \frac{\partial n}{\partial T} d\omega \,. \tag{35}$$

We show calculations of Eq. (35) as a function of n_p in Fig. 19. The predicted κ from Eq. (35) agrees well with the experimental data, yet we emphasize that no *a priori* knowledge of the bulk phase thermal conductivity is needed in the calculations of Eq. (35), unlike the effective medium theories.[40] The only required inputs to our "porous minimum limit" calculations are bulk number density and bulk sound velocity. As further validation of the predictive power of our "porous minimum limit," we plot the predictive κ as a function of T in Fig. 20 along with data on the two aerogel thin films from our TDTR analysis. Our porous minimum limit agrees well with the measured thermal conductivities of the aerogel films. Also, our aerogel films exhibit a very similar temperature dependence in κ as bulk SiO$_2$, indicating that confinement is not affecting the thermal vibrations over our temperature range. For comparison, also shown in Fig. 20 are the measured thermal conductivities of the cover glass substrate (VWR Cover Glass # 48368040) compared to previously measured Corning Pyrex #7740 and bulk SiO_2.[20,49]

In summary, we have measured the thermal conductivity of aerogel thin-films with TDTR. The reduced thermal conductivity in the porous silica structures is ascribed to a reduced sound velocity from that of bulk silica glass. From this, a minimum limit to thermal conductivity for porous materials is derived that agrees well with our experimental data.

5. CONCLUSIONS

Thermal management has assumed a critical role in the design and development of electronic devices, power generation modules, and waste energy harvesting techniques. In these applications, performance depends vitally on the thermal conductivity (κ) of the component materials. However, as length scales of nanomaterials approach thermal carrier mean free paths and wavelengths, the thermal transport in nanosystems becomes primarily driven by the conduction of energy across material interfaces, characterized by the thermal boundary conductance.

The overarching goal of this Truman LDRD project was to explore mechanisms of thermal transport at interfaces of nanomaterials, specifically linking the thermal conductivity and thermal boundary conductance to the structures and geometries of interfaces and boundaries. An understanding of the physics of energy carrier scattering processes and their response to interfacial disorder will elucidate the potentials of applying these novel materials to next-generation high powered nanodevices and energy conversion applications. An additional goal of this project was to use the knowledge gained from linking interfacial structure to thermal transport in order to develop avenues to control, or “tune” the thermal transport in nanosystems.

One of the major accomplishments of this Truman LDRD was the development of time domain thermoreflectance (TDTR), a short pulsed laser technique that can measure the thermal conductivity and thermal boundary conductance in nanomaterials and nanosystems. This technique was used to explore the effects of electron-phonon, phonon-phonon, and interface scattering in a wide array of nanomaterials. In addition to the experimental work, several new theories describing thermal carrier interactions on the nanoscale have been developed. These experimental and theoretical projects from this LDRD have resulted in 38 refereed journal publications, with an additional 3 publications currently under review, and 1 invited book chapter. This SAND report only discussed a few of these publications in depth (2 published and the 2 currently under review – c.f. Section 4). A full list of all the journal publications is given in the Appendix.

6. REFERENCES

1. A. Majumdar, "Lower limit of thermal conductivity: Diffusion versus localization," Microscale Thermophysical Engineering **2,** 5-9 (1998).
2. G. Chen, *Nanoscale Energy Transport and Conversion: A Parallel Treatment of Electrons, Molecules, Phonons, and Photons* (Oxford University Press, New York, 2005).
3. D. G. Cahill, W. K. Ford, K. E. Goodson, G. D. Mahan, A. Majumdar, H. J. Maris, R. Merlin, and S. R. Phillpot, "Nanoscale thermal transport," J. Appl. Phys. **93,** 793-818 (2003).
4. E. Pop, "Energy dissipation and transport in nanoscale devices," Nano Research **3,** 147-169 (2010).
5. G. J. Snyder, and E. S. Toberer, "Complex thermoelectric materials," Nature Materials **7,** 105-114 (2008).
6. G. Pernot, M. Stoffel, I. Savic, F. Pezzoli, P. Chen, G. Savelli, A. Jacquot, J. Schumann, U. Denker, I. Monch, C. Deneke, O. G. Schmidt, J. M. Rampnoux, S. Wang, M. Plissonnier, A. Rastelli, S. Dilhaire, and N. Mingo, "Precise control of thermal conductivity at the nanoscale through individual phonon-scattering barriers," Nature Materials **9,** 491-495 (2010).
7. B. C. Gundrum, D. G. Cahill, and R. S. Averback, "Thermal conductance of metal-metal interfaces," Phys. Rev. B **72,** 245426 (2005).
8. P. E. Hopkins, T. E. Beechem, J. C. Duda, J. L. Smoyer, and P. M. Norris, "Effects of subconduction band excitations on thermal conductance at metal-metal interfaces," Appl. Phys. Lett. **96,** 011907 (2010).
9. A. Majumdar, and P. Reddy, "Role of electron-phonon coupling in thermal conductance of metal-nonmetal interfaces," Appl. Phys. Lett. **84,** 4768-4770 (2004).
10. A. V. Sergeev, "Electronic Kapitza conductance due to inelastic electron-boundary scattering," Phys. Rev. B **58,** R10199 (1998).
11. A. V. Sergeev, "Inelastic electron-boundary scattering in thin films," Physica B **263-264,** 217-219 (1999).
12. E. T. Swartz, and R. O. Pohl, "Thermal boundary resistance," Reviews of Modern Physics **61,** 605-668 (1989).
13. R. M. Costescu, M. A. Wall, and D. G. Cahill, "Thermal conductance of epitaxial interfaces," Phys. Rev. B **67,** 054302 (2003).
14. R. J. Stoner, and H. J. Maris, "Kapitza conductance and heat flow between solids at temperatures from 50 to 300 K," Phys. Rev. B **48,** 16373-16387 (1993).
15. P. E. Hopkins, J. C. Duda, C. W. Petz, and J. A. Floro, "Controlling thermal conductance through quantum dot roughening at interfaces," Phys. Rev. B**,** (to appear).
16. Z. Chen, W. Jang, W. Bao, C. N. Lau, and C. Dames, "Thermal contact resistance between graphene and silicon dioxide," Appl. Phys. Lett. **95,** 161910 (2009).
17. H.-K. Lyeo, and D. G. Cahill, "Thermal conductance of interfaces between highly dissimilar materials," Phys. Rev. B **73,** 144301 (2006).
18. Y. K. Koh, M.-K. Bae, D. G. Cahill, and E. Pop, "Heat conduction across monolayer and few layer graphenes," Nano Letters **10,** 4363-4368 (2010).
19. P. E. Hopkins, J. C. Duda, S. P. Clark, C. P. Hains, T. J. Rotter, L. M. Phinney, and G. Balakrishnan, "Effect of dislocation density on thermal boundary conductance across GaSb/GaAs interfaces," Appl. Phys. Lett. **98,** 161913 (2011).

20. D. G. Cahill, "Thermal conductivity measurement from 30 to 750 K: the 3ω method," Review of Scientific Instruments **61,** 802-808 (1990).
21. P. E. Hopkins, P. M. Norris, R. J. Stevens, T. Beechem, and S. Graham, "Influence of interfacial mixing on thermal boundary conductance across a chromium/silicon interface," J. Heat Transfer **130,** 062402 (2008).
22. P. E. Hopkins, L. M. Phinney, J. R. Serrano, and T. E. Beechem, "Effects of surface roughness and oxide layer on the thermal boundary conductance at aluminum/silicon interfaces," Phys. Rev. B **82,** 085307 (2010).
23. P. E. Hopkins, K. Hattar, T. Beechem, J. F. Ihlefeld, D. L. Medlin, and E. S. Piekos, "Reduction in thermal boundary conductance due to proton implantation in silicon and sapphire," Appl. Phys. Lett. **98,** 231901 (2011).
24. T. E. Beechem, S. Graham, P. E. Hopkins, and P. M. Norris, "The role of interface disorder on thermal boundary conductance using a virtual crystal approach," Appl. Phys. Lett. **90,** 054104 (2007).
25. T. Beechem, and P. E. Hopkins, "Predictions of thermal boundary conductance for systems of disordered solids and interfaces," J. Appl. Phys. **106,** 124301 (2009).
26. C. A. Paddock, and G. L. Eesley, "Transient thermoreflectance from thin metal films," J. Appl. Phys. **60,** 285-290 (1986).
27. Y. K. Koh, and D. G. Cahill, "Frequency dependence of the thermal conductivity of semiconductor alloys," Phys. Rev. B **76,** 075207 (2007).
28. H.-K. Lyeo, D. G. Cahill, B.-S. Lee, and J. R. Abelson, "Thermal conductivity of phase-change material $Ge_2Sb_2Te_5$," Appl. Phys. Lett. **89,** 151904 (2006).
29. A. J. Schmidt, X. Chen, and G. Chen, "Pulse accumulation, radial heat conduction, and anisotropic thermal conductivity in pump-probe transient thermoreflectance," Review of Scientific Instruments **79,** 114902 (2008).
30. W. S. Capinski, H. J. Maris, T. Ruf, M. Cardona, K. Ploog, and D. S. Katzer, "Thermal-conductivity measurements of GaAs/AlAs superlattices using a picosecond optical pump-and-probe technique," Phys. Rev. B **59,** 8105-8113 (1999).
31. C. Chiritescu, D. G. Cahill, N. Nguyen, D. Johnson, A. Bodapati, P. Keblinski, and P. Zschack, "Ultralow thermal conductivity in disordered, layered WSe_2 crystals," Science **315,** 351-353 (2007).
32. R. M. Costescu, D. G. Cahill, F. H. Fabreguette, Z. A. Sechrist, and S. M. George, "Ultra-low thermal conductivity in W/Al_2O_3 nanolaminates," Science **303,** 989-990 (2004).
33. P. E. Hopkins, R. J. Stevens, and P. M. Norris, "Influence of inelastic scattering at metal-dielectric interfaces," J. Heat Transfer **130,** 022401 (2008).
34. R. J. Stevens, A. N. Smith, and P. M. Norris, "Measurement of thermal boundary conductance of a series of metal-dielectric interfaces by the Transient Thermoreflectance Technique," J. Heat Transfer **127,** 315-322 (2005).
35. A. Schmidt, M. Chiesa, X. Chen, and G. Chen, "An optical pump-probe technique for measuring the thermal conductivity of liquids," Review of Scientific Instruments **79,** 064902 (2008).
36. D. G. Cahill, "Analysis of heat flow in layered structures for time-domain thermoreflectance," Review of Scientific Instruments **75,** 5119-5122 (2004).
37. H. S. Carslaw, and J. C. Jaeger, "Section 3.7. Steady periodic temperature in composite slabs, pp. 109-112," in *Conduction of Heat in Solids, 2nd (2003) Ed.,* (Oxford University Press, New York, 1959), pp. 109-112.

38. A. Feldman, "Algorithm for solutions of the thermal diffusion equation in a stratified medium with a modulated heating source," High Temperatures-High Pressures **31,** 293-298 (1999).

39. C. Chiritescu, D. G. Cahill, C. Heibeman, Q. Lin, c. Mortensen, N. T. Nguyen, D. Johnson, R. Rostek, and H. Bottner, "Low thermal conductivity in nanoscale layered materials synthesized by the method of modulated elemental reactants," J. Appl. Phys. **104,** 033503 (2008).

40. R. M. Costescu, A. J. Bullen, G. Matamis, K. E. O'Hara, and D. G. Cahill, "Thermal conductivity and sound velocities of hydrogen-silsequioxane low-*k* dielectrics," Phys. Rev. B **65,** 094205 (2002).

41. Y. K. Koh, Y. Cao, D. G. Cahill, and D. Jena, "Heat-transport mechanisms in superlattices," Adv. Func. Mat. **19,** 610-615 (2009).

42. P. E. Hopkins, "Effects of electron-boundary scattering on changes in thermoreflectance in thin metal films undergoing intraband transitions," J. Appl. Phys. **105,** 093517 (2009).

43. Y. Ezzahri, S. Grauby, S. Dilhaire, J. M. Rampnoux, and W. Claeys, "Cross-plan Si/SiGe superlattice acoustic and thermal properties measurement by picosecond ultrasonics," J. Appl. Phys. **101,** 013705 (2007).

44. D. G. Cahill, K. E. Goodson, and A. Majumdar, "Thermometry and thermal transport in micro/nanoscale solid-state devices and structures," J. Heat Transfer **124,** 223-241 (2002).

45. R. J. Stevens, A. N. Smith, and P. M. Norris, "Signal analysis and characterization of experimental setup for the transient thermoreflectance technique," Review of Scientific Instruments **77,** 084901 (2006).

46. A. J. Schmidt, "Optical characterization of thermal transport from the nanoscale to the macroscale," in *Mechanical Engineering,* (Massachusetts Institute of Technology, Cambridge, MA, USA, 2008).

47. A. J. Schmidt, R. Cheaito, and M. Chiesa, "A frequency-domain thermoreflectance method for the characterization of thermal properties," Review of Scientific Instruments **80,** 094901 (2009).

48. P. E. Hopkins, J. R. Serrano, L. M. Phinney, S. P. Kearney, T. W. Grasser, and C. T. Harris, "Criteria for cross-plane dominated thermal transport in multilayer thin film systems during modulated laser heating," J. Heat Transfer **132,** 081302 (2010).

49. F. Incropera, and D. P. DeWitt, *Fundamentals of Heat and Mass Transfer* (Wiley and Sons, Inc., New York, 1996).

50. C. Thomsen, J. Strait, Z. Vardeny, H. J. Maris, J. Tauc, and J. J. Hauser, "Coherent phonon generation and detection by picosecond light pulses," Phys. Rev. Lett. **53,** 989-992 (1984).

51. C. Thomsen, H. T. Grahn, H. J. Maris, and J. Tauc, "Surafce generation and detection of phonons by picosecond light pulses," Phys. Rev. B **34,** 4129-4138 (1986).

52. W. Kim, J. Zide, A. Gossard, D. Klenov, S. Stemmer, A. Shakouri, and A. Majumdar, "Thermal conductivity reduction and thermoelectric figure of merit increase by embedding nanoparticles in crystalline semiconductors," Phys. Rev. Lett. **96,** 045901 (2006).

53. G. Zeng, J.-H. Bahk, J. E. Bowers, J. M. O. Zide, A. C. Gossard, Z. Bian, R. Singh, A. Shakouri, W. Kim, S. L. Singer, and A. Majumdar, "ErAs:$(InGaAs)_{1-x}(InAlAs)_x$ alloy power generator modules," Appl. Phys. Lett. **91,** 263510 (2007).

54. Y. K. Koh, S. L. Singer, W. Kim, J. M. O. Zide, H. Lu, D. G. Cahill, A. Majumdar, and A. C. Gossard, "Comparison of the 3ω method and time-domain thermoreflectance for measurements of the cross-plane thermal conductivity of epitaxial semiconductors," J. Appl. Phys. **105,** 054303 (2009).
55. X. J. Hu, R. Prasher, and K. Lofgreen, "Ultralow thermal conductivity of nanoparticle packed bed," Appl. Phys. Lett. **91,** 203113 (2007).
56. J.-H. Lee, G. A. Galli, and J. C. Grossman, "Nanoporous Si as an efficient thermoelectric material," Nano Letters **8,** 3750-3754 (2008).
57. R. S. Prasher, "Ultralow thermal conductivity of a packed bed of cystalline nanoparticles: A theoretical study," Phys. Rev. B **74,** 165413 (2006).
58. R. Venkatasubramanian, E. Siivola, T. Colpittas, and B. O'Quinn, "Thin-film thermoelectric devices with high room-temperature figures of merit," Nature **413,** 597-602 (2001).
59. S.-M. Lee, D. G. Cahill, and R. Venkatasubramanian, "Thermal conductivity of Si-Ge superlattices," Appl. Phys. Lett. **70,** 2957-2959 (1997).
60. J.-K. Yu, S. Mitrovic, D. Tham, J. Varghese, and J. R. Heath, "Reduction of thermal conductivity in phononic nanomesh structures," Nature Nanotechnology **5,** 718-721 (2010).
61. S. T. Huxtable, A. R. Abramson, C. L. Tien, A. Majumdar, C. LaBounty, X. Fan, G. Zeng, J. E. Bowers, A. Shakouri, and E. T. Croke, "Thermal conductivity of Si/SiGe and SiGe/SiGe superlattices," Appl. Phys. Lett. **80,** 1737-1739 (2002).
62. B. Poudel, Q. Hao, Y. Ma, L. Yucheng, A. Minnich, B. Yu, X. Yan, D. Wang, A. Muto, D. Vashaee, X. Chen, J. Liu, M. S. Dresselhaus, G. Chen, and Z. Ren, "High-thermoelectric performance of nanostructured bismuth antimony telluride bulk alloys," Science **320,** 634-638 (2008).
63. L. E. Bell, "Cooling, heating, generating power, and recovering waste heat with thermoelectric systems," Science **321,** 1457-1461 (2008).
64. T. C. Harman, P. J. Taylor, M. P. Walsh, and B. E. LaForge, "Quantum dot superlattice thermoelectric materials and devices," Science **297,** 2229-2232 (2002).
65. N. P. Padture, M. Gell, and E. H. Jordan, "Thermal barrier coatings for gas-turbing engine applications," Science **296,** 280-284 (2002).
66. B. Yang, J. L. Liu, K. L. Wang, and G. Chen, "Simultaneous measurements of Seebeck coefficient and thermal conductivity across superlattice," Appl. Phys. Lett. **80,** 1758-1760 (2002).
67. M. L. Lee, and R. Venkatasubramanian, "Effect of nanodot areal density and period on thermal conductivity in SiGe/Si nanodot superlattices," Appl. Phys. Lett. **92,** 053112 (2008).
68. D. J. Eaglesham, and M. Cerullo, "Dislocation-free Stranski-Krastanow growth of Ge on Si(100)," Phys. Rev. Lett. **64,** 1943-1946 (1990).
69. G. Medeiros-Ribeiro, A. M. Bratkovski, T. I. Kamins, D. A. Ohlberg, and R. S. Williams, "Shape transition of germanium nanocrystals on a silicon (001) surface from pyramids to domes," Science **279,** 353-355 (1998).
70. T. Kamins, G. Medeiros-Ribeiro, D. Ohlberg, and R. S. Williams, "Dome-to-pyramid transition included by alloying of Ge islands on Si(001)," Applied Physics A: Materials Science and Processing **67,** 727-730 (1998).

71. F. M. Ross, J. Tersoff, and R. M. Tromp, "Coarsening of self-assembled Ge quantum dots on Si(001)," Phys. Rev. Lett. **80,** 984-987 (1998).
72. B. Cho, T. Schwarz-Selinger, K. Ohmori, D. G. Cahill, and J. E. Greene, "Effect of growth rate on the spatial distributions of dome-shaped Ge islands on Si(001)," Phys. Rev. B **66,** 195407 (2002).
73. M. W. Dashiell, U. Denker, C. Muller, G. Costantini, C. Manzano, K. Kern, and O. G. Schmidt, "Photoluminescence of ultrasmall Ge quantum dots grown by molecular-beam epitaxy at low temperatures," Appl. Phys. Lett. **80,** 1279-1281 (2002).
74. J. C. Duda, T. Beechem, J. L. Smoyer, P. M. Norris, and P. E. Hopkins, "The role of dispersion on phononic thermal boundary conductance," J. Appl. Phys. **108,** 073515 (2010).
75. G. Gilat, and R. M. Nicklow, "Normal vibrations in aluminum and derived thermodynamic properties," Phys. Rev. **143,** 487-494 (1966).
76. W. Weber, "Atomic bond charge model for the phonons in diamond, Si, Ge, and α-Sn," Phys. Rev. B **15,** 4789-4803 (1977).
77. E. S. Landry, and A. J. H. McGaughey, "Thermal boundary resistance predictions from molecular dynamics simulations and theoretical calculations," Phys. Rev. B **80,** 165304 (2009).
78. J. C. Duda, P. E. Hopkins, J. L. Smoyer, M. L. Bauer, T. S. English, C. B. Saltonstall, and P. M. Norris, "On the assumption of detailed balance in prediction of diffusive transmission probability during interfacial transport," Nanoscale and Microscale Thermophysical Engineering **14,** 21-33 (2010).
79. D. G. Cahill, and R. O. Pohl, "Thermal conductivity of amorphous solids above the plateau," Phys. Rev. B **35,** 4067-4073 (1987).
80. R. C. Zeller, and R. O. Pohl, "Thermal conductivity and specific heat of noncrystalline solids," Phys. Rev. B **4,** 2029-2041 (1971).
81. S. P. Hepplestone, and G. P. Srivastava, "Theory of interface scattering of phonons in superlattices," Phys. Rev. B **82,** 144303 (2010).
82. S. Shin, M. Kaviany, T. Desai, and R. Bonner, "Roles of atomic restructuring in interfacial phonon transport," Phys. Rev. B **82,** 081302 (2010).
83. P. K. Schelling, S. R. Phillpot, and P. Keblinski, "Kapitza conductance and phonon scattering at grain boundaries by simulation," J. Appl. Phys. **95,** 6082-6091 (2004).
84. A. H. Castro Neto, F. Guinea, N. M. R. Peres, K. S. Novoselov, and A. K. Geim, "The electronic properties of graphene," Reviews of Modern Physics **81,** 109-162 (2009).
85. N. M. R. Peres, "*Colloquim*: The transport properties of graphene: An introduction," Reviews of Modern Physics **82,** 2673-2700 (2010).
86. A. A. Balandin, S. Ghosh, W. Bao, I. Calizo, D. Teweldebrhan, F. Miao, and C. N. Lau, "Superior thermal conductivity of single-layer graphene," Nano Letters **8,** 902-907 (2008).
87. Z. Wang, R. Xie, C. T. Bui, D. Liu, X. Ni, B. Li, and J. T. L. Thong, "Thermal transport in suspended and supported few-layer graphene," Nano Letters **11,** 113-118 (2011).
88. S. Ghosh, W. Bao, D. L. Nika, S. Subrina, E. P. Pokatilov, C. N. Lau, and A. A. Balandin, "Dimensional crossover of thermal transport in few-layer graphene," Nature Materials **9,** 555-558 (2010).

89. J. H. Seol, I. Jo, A. L. Moore, L. Lindsay, Z. H. Aitken, M. T. Pettes, X. Li, Z. Yao, R. Huang, D. A. Broido, N. Mingo, R. S. Ruoff, and L. Shi, "Two-dimensional phonon transport in supported graphene," Science **328,** 213-216 (2010).
90. P. L. Kapitza, "The study of heat transer in Helium II," Zhurnal eksperimentalnoi i teoreticheskoi fiziki **11,** 1-31 (1941).
91. P. M. Norris, and P. E. Hopkins, "Examining interfacial diffuse phonon scattering through transient thermoreflectance measurements of thermal boundary conductance," J. Heat Transfer **131,** 043207 (2009).
92. W. Cai, A. L. Moore, Y. Zhu, X. Li, S. Chen, L. Shi, and R. S. Ruoff, "Thermal transport in suspended and supported monolayer graphene grown by chemical vapor deposition," Nano Letters **10,** 1645-1651 (2010).
93. E. T. Swartz, and R. O. Pohl, "Thermal Boundary Resistance," Review of Modern Physics **61,** 605-665 (1989).
94. A. J. Schmidt, K. C. Collins, A. J. Minnich, and G. Chen, "Thermal conductance and phonon tranmissivity of metal-graphte interfaces," J. Appl. Phys. **107,** 104907 (2010).
95. X. Li, W. Cai, J. An, S. Kim, J. Nah, D. Yang, R. Piner, A. Velamakanni, I. Jung, E. Tutuc, S. K. Banerjee, L. Colombo, and R. S. Ruoff, "Large-area synthesis of high-quality and uniform graphene films on copper foils," Science **324,** 1312-1314 (2009).
96. M. Baraket, S. G. Walton, E. H. Lock, J. T. Robinson, and F. K. Perkins, "The functionalization of graphene using elecron-beam generated plasmas," Appl. Phys. Lett. **96,** 231501 (2010).
97. A. C. Ferrari, J. C. Meyer, V. Scardaci, C. Casiraghi, M. Lazzeri, F. Mauri, S. Piscanec, D. Jiang, K. S. Novoselov, S. Roth, and A. K. Geim, "Ramam spectrum of graphene and graphene layers," Phys. Rev. B **97,** 187401 (2006).
98. L. G. Cancado, A. Jorio, E. H. Martins Ferreira, F. Stavale, C. A. Achete, R. B. Capaz, M. V. O. Moutinho, A. Lombardo, T. S. Kulmala, and A. C. Ferrari, "Quantifying defects in graphene via Raman spectroscopy at different excitation energies," Nano Letters **Article ASAP,** DOI: 10.1021/nl201432g (2011).
99. T. M. G. Mohiuddin, A. Lombardo, R. R. Nair, A. Bonetti, G. Savini, R. Jalil, N. Bonini, D. M. Basko, C. Galiotis, N. Marzari, K. S. Novoselov, A. K. Geim, and A. C. Ferrari, "Uniaxial strain in graphene by Raman spectroscopy: G peak splitting, Gruneisen parameters, and sample orientation," Phys. Rev. B **79,** 205433 (2009).
100. A. Das, B. Chakraborty, S. Piscanec, S. Pisana, A. K. Sood, and A. C. Ferrari, "Phonon renormalization in doped bilayer graphene," Phys. Rev. B **79,** 155417 (2009).
101. B. Lee, S.-Y. Park, H.-C. Kim, K. Cho, E. M. Vogel, M. J. Kim, R. M. Wallace, and J. Kim, "Conformal Al_2O_3 dielectric layer deposited by atomic layer deposition for graphene-based nanoelectronics," Appl. Phys. Lett. **92,** 203102 (2008).
102. H. Wang, J.-P. Griffiths, R. G. Egdell, M. G. Moloney, and J. S. Foord, "Chemical functionalizatino of diamond surfaces by raction with diaryl carbenes," Langmuir **24,** 862-868 (2008).
103. J. Kim, and T. W. Kim, "Initial surface reactions of atomic layer deposition," JOM Journal of Minerals, Metals and Materials Society **61,** 17-22 (2009).
104. S. G. Walton, E. H. Lock, M. Baraket, P. E. Sheehan, Z. Wei, J. T. Robinson, and E. S. Snow, "Plasma-based approach to controlling the oxygen concentration in graphene oxide," in *Society of Vacuum Coaters 52nd Annual Technical Conference*, (Santa Clara, 2009).

105. R. J. Stoner, H. J. Maris, T. R. Anthony, and W. F. Banholzer, "Measurements of the Kapitza conductance between diamond and several metals," Phys. Rev. Lett. **68,** 1563-1566 (1992).
106. K. C. Collins, and G. Chen, "Effects of surface chemistry on thermal conductance at aluminum-diamond interfaces," Appl. Phys. Lett. **97,** 083102 (2010).
107. J. C. Duda, J. L. Smoyer, P. M. Norris, and P. E. Hopkins, "Extension of the diffuse mismatch model for thermal boundary conductance between isotropic and anisotropic materials," Appl. Phys. Lett. **95,** 031912 (2009).
108. W. G. Vincenti, and C. H. Kruger, *Introduction to Physical Gas Dynamics* (Krieger Publishing Company, Malabar, FL, 2002).
109. R. Nicklow, N. Wakabayashi, and H. G. Smith, "Lattice dynamics of pyrolytic graphite," Phys. Rev. B **5,** 4951-4962 (1972).
110. S. Viola Kusminskiy, D. K. Campbell, and A. H. Castro Neto, "Lenosky's energy and the phonon dispersion of graphene," Phys. Rev. B **80,** 035401 (2009).
111. W. Jang, Z. Chen, W. Bao, C. N. Lau, and C. Dames, "Thickness-dependent thermal conductivity of encased graphene and ultrathin graphene," Nano Letters **10,** 3909-3913 (2010).
112. D. G. Cahill, S. K. Watson, and R. O. Pohl, "Lower limit to the thermal conductivity of disordered crystals," Phys. Rev. B **46,** 6131-6140 (1992).
113. C. W. Chang, D. Okawa, A. Majumdar, and A. Zettl, "Solid-state thermal rectifier," Science **314,** 1121-1124 (2006).
114. C. Dames, "Solid-state thermal rectification with existing bulk materials," J. Heat Transfer **131,** 061301 (2009).
115. P. E. Hopkins, and J. R. Serrano, "Phonon localization and thermal rectification in asymmetric harmonic chains using a nonequilibrium Green's function formalism," Phys. Rev. B **80,** 201408(R) (2009).
116. B. Hu, L. Yang, and Y. Zhang, "Asymmetric heat conduction in nonlinear lattices," Phys. Rev. Lett. **97,** 124302 (2006).
117. B. Li, L. Wang, and G. Casati, "Negative differential thermal resistance and thermal transistor," Appl. Phys. Lett. **88,** 143501 (2006).
118. L. Wang, and B. Li, "Thermal memory: A storage for phononic information," Phys. Rev. Lett. **101,** 267203 (2008).
119. P. M. Norris, A. P. Caffrey, R. J. Stevens, J. M. Klopf, J. T. McLeskey, and A. N. Smith, "Femtosecond pump-probe nondestructive examination of materials," Review of Scientific Instruments **74,** 400-406 (2003).
120. T. Sugimoto, X. W. Zhou, and A. Muramatsu, "Synthesis of uniform anatase TiO2 nanoparticles by gel-sol method 4. Shape control," Journal of Colloid and Interface Science **259,** 53-61 (2003).
121. M. Mittal, and E. M. Furst, "Electric field-directed convective assembly of ellipsoidal colloidal particles to create optically and mechanically anisotropic thin films," Adv. Func. Mat. **19,** 3271-3278 (2009).
122. M. Mittal, R. K. Niles, and E. M. Furst, "Flow-directed assembly of anisotropic titania particles," Nanoscale **2,** 2237-2243 (2010).
123. P. E. Hopkins, B. Kaehr, L. M. Phinney, T. P. Koehler, A. M. Grillet, D. Dunphy, F. Garcia, and C. J. Brinker, "Measuring the thermal conductivity of porous, transparent SiO_2 films with time domain thermoreflectance," J. Heat Transfer **133,** 061601 (2011).

124. *Thermal Conductivitiy - Nonmetallic Solids* (IFI/Plenum, New York, 1970).
125. S.-M. Lee, D. G. Cahill, and T. H. Allen, "Thermal conductivity of sputtered oxide films," Phys. Rev. B **52,** 253-257 (1995).
126. D. G. Cahill, and T. H. Allen, "Thermal conductivity of sputtered and evaporated SiO_2 and TiO_2 optical coatings," Appl. Phys. Lett. **65,** 309-311 (1994).
127. J. Callaway, "Model for lattice thermal conductivity at low temperatures," Phys. Rev. **113,** 1046-1051 (1959).
128. M. G. Holland, "Analysis of lattice thermal conductivity," Phys. Rev. **132,** 2461-2471 (1963).
129. N. Mingo, "Calculation of Si nanowire thermal conductivity using complete phonon dispersion relation," Phys. Rev. B **68,** 113308 (2003).
130. A. Einstein, "Elementary observations on thermal molecular motion in solids," Ann. Phys. **35,** 679-694 (1911).
131. D. G. Cahill, and R. O. Pohl, "Heat flow and lattice vibrations in glasses," Solid State Commun. **70,** 927-930 (1989).
132. D. G. Cahill, and R. O. Pohl, "Lattice vibrations and heat transport in crystals and glasses," Ann. Rev. Phys. Chem. **39,** 93-121 (1988).
133. S.-M. Lee, and D. G. Cahill, "Heat transport in thin dielectric films," J. Appl. Phys. **81,** 2590-2595 (1997).
134. P. E. Hopkins, and T. Beechem, "Phonon scattering and velocity considerations in the minimum phonon thermal conductivity of layered solids above the plateau," Nanoscale and Microscale Thermophysical Engineering **14,** 51-61 (2010).
135. B. D. Gates, Q. Xu, M. Stewart, M. Ryan, C. G. Willson, and G. M. Whitesides, "New approaches to nanofabrication: molding, printing, and other techniques," Chemical Reviews **105,** 1171-1196 (2005).
136. C. J. Brinker, Y.-C. Lu, A. Sellinger, and H. Fan, "Evaporation-induced self-assembly: nanostructures made easy," Advanced Materials **11,** 579-585 (1999).
137. L. W. Hrubesh, and R. W. Pekala, "Thermal properties of organic and inorganic aerogels," J. Mater. Res. **9,** 731-738 (1994).
138. E. Hummer, X. Lu, T. Rettelbach, and J. Fricke, "Heat transfer in opacified aerogel powders," Journal of Non-Crystalline Solids **145,** 211-216 (1992).
139. S. Spagnol, B. Lartigue, and A. Trombe, "Experimental investigations on the thermal conductivity of silica aerogels by a guarded thin-film-heater method," J. Heat Transfer **131,** 074501 (2009).
140. J. Fricke, X. Lu, P. Wang, D. Buttner, and U. Heinemann, "Optimization of monolithic silica aerogel insulants," Int. J. Heat and Mass Transfer **35,** 2305-2309 (1992).
141. S. S. Prakash, C. J. Brinker, and A. J. Hurd, "Silica aerogel films at ambient pressure," Journal of Non-Crystalline Solids **190,** 264-275 (1995).
142. A. I. Persson, Y. K. Koh, D. G. Cahill, L. Samuelson, and H. Linke, "Thermal conductance of InAs nanowire composites," Nano Letters **9,** 4484-4488 (2009).
143. P. Scheuerpflug, M. Hauck, and J. Fricke, "Thermal properties of silica aerogels between 1.4 and 330 K," Journal of Non-Crystalline Solids **145,** 196-201 (1992).
144. M. Kaviany, *Principles of Heat Transfer in Porous Media* (Springer-Verlag, New York, 1991).

145. T.-Y. Wei, S.-Y. Lu, and Y.-C. chang, "A new class of opacified monolithic aerogels of ultralow high-temperature thermal conductivities," Journal of Physical Chemistry C **113,** 7424-7428 (2009).

146. d. u. m. f. o. t. g. m. w. t. a. The overall density of the aerogel film was 1.15 g/cm^3 using a Bruggeman effective medium approximation.

147. A. J. Ricco, G. C. Frye, and S. J. Martin, "Determination of BET surface areas of porous thin films using surface acoustic wave techniques," Langmuir **5,** 273-276 (1989).

APPENDIX: LIST OF PUBLISHED PAPERS FROM LDRD

Book Chapters
1. Hopkins, P.E, Duda, J.C., "Introduction to Nanoscale Thermal Conduction," in *Heat Transfer – Mathematical Modelling, Numerical Methods, and Information Technology*, Belmiloudi, A. (Ed.), InTech, pp. 305 – 330, ISBN: 978-953-307-550-1 (2011). *Invited and open access (*http://www.intechopen.com/articles/show/title/introduction-to-nanoscale-thermal-conduction*).*

Journal Publications
Under review
41. Hopkins, P.E., Baraket, M., Barnat, E.V., Beechem, T.E., Kearney, S.P., Robinson, J.T., Walton, S.G., "Manipulating thermal conductance at metal-graphene contacts via the chemical modification of graphene."

40. Hopkins, P.E., Kaehr, B., Piekos, E.S., Dunphy, D., Brinker, C.J., "Minimum thermal conductivity considerations in aerogel thin films."

Published
39. Hopkins, P.E., Mittal, M., Phinney, L.M., Grillet, A.M., Furst, E.M., "Ultra-low thermal conductivity of ellipsoidal TiO_2 nanoparticle films," *Applied Physics Letters* **99**, 133106 (2011).

38. Hopkins, P.E., Beechem, T.E., Duda, J.C., Hattar, K., Ihlefeld, J.F., Rodriguez, M.A., Piekos, E.S., "Influence of anisotropy on thermal boundary conductance at solid interfaces," *Physical Review B* **84**, (2011).

37. Hopkins, P.E., Duda, J.C., Petz, C.W., Floro, J.A., "Controlling thermal conductance through quantum dot roughening at interfaces," *Physical Review B* **84**, 035438 (2011) – *Selected to appear in the Virtual Journal of Nanoscale Science and Technology, volume 24, issue 6.*

36. Hopkins, P.E., Hattar, K., Beechem, T., Ihlefled, J.F., Medlin, D.L., Piekos, E.S., "Reduction in thermal boundary conductance due to proton implantation in silicon and sapphire," *Applied Physics Letters* **98**, 231901 (2011).

35. Hopkins, P.E., Duda, J.C., Clark, S.P., Hains, C.P., Rotter, T.J., Phinney, L.M., Balakrishnan, G., "Effect of dislocation density on the thermal boundary conductance across GaSb/GaAs interfaces," *Applied Physics Letters* **98**, 161913 (2011).

34. Hopkins, P.E., Phinney, L.M., Rakich, P.T., Olsson, R.H., El-Kady, I., "Phonon considerations in the reduction of thermal conductivity in phononic crystals," *Applied Physics A* **103**, 575-579 (2011).

33. Ahirwar, P., Clark, S., Jaeckel, F., Hains, C., Albrecht, A., Schjetnan, P., Rotter, T.J., Dawson, L.R., Balakrishnan, G., Phinney, L., Hopkins, P.E., Hader, J., Moloney, J.V., "Growth and thermal conductivity analysis of poly-crystalline GaAs on CVD diamond for use in thermal

management of high-power semiconductor lasers," *Journal of Vacuum Science and Technology B* **29**, 03C130 (2011).

32. Duda, J.C., Norris, P.M., Hopkins, P.E., "Origin of the temperature dependency of interfacial transport in the classical limit," *Journal of Heat Transfer* 133, 074501 (2011).

31. Duda, J.C., Saltonstall, C.B., Norris, P.M., Hopkins, P.E., "Assessment and prediction of thermal transport at solid-SAM junctions," *Journal of Chemical Physics* 134, 094704 (2011).

30. Hopkins, P.E., Kaehr, B.J., Phinney, L.M., Koehler, T.P., Grillet, A.M., Dunphy, D., Garcia, F., Brinker, C.J., "Measuring the thermal conductivity of porous, transparent SiO_2 films with time domain thermoreflectance," *Journal of Heat Transfer* 133, 061601 (2011).

29. Hopkins, P.E., Duda, J.C., Norris, P.M., "Anharmonic phonon interactions at interfaces and contributions to thermal boundary conductance," *Journal of Heat Transfer* 133, 062401 (2011).

28. Hopkins, P.E., Phinney, L.M., Serrano, J.R., "Re-examining electron-Fermi relaxation in Au with a nonlinear thermoreflectance model," *Journal of Heat Transfer* 133, 044505 (2011).

27. Hopkins, P.E., Reinke, C.M., Su, M.F., Olsson, R.H., Shaner, E.A., Leseman, Z.C., Serrano, J.R., Phinney, L.M., El-Kady, I., "Reduction in the thermal conductivity of single crystalline silicon by phononic crystal patterning," *Nano Letters* 11, 107-112 (2011).

26. Hopkins, P.E., Serrano, J.R., Phinney, L.M., Li, H., Picraux, S.T., Misra, A., "Boundary scattering effects during electron thermalization in nanoporous gold," *Journal of Applied Physics* 109, 013524 (2011) – *Selected for the February 2011 issue of the Virtual Journal of Ultrafast Science*.

25. Hopkins, P.E., Serrano, J.R., Phinney, L.M., "Comparison of thermal conductivity and thermal boundary conductance measurements using continuous-wave and ultrashort-pulsed thermoreflectance techniques," *International Journal of Thermophysics* 31, 2380 (2010).

24. Hopkins, P.E., Bauer, M.L., Duda, J.C., Smoyer, J.L., English, T. S., Norris, P.M., Beechem, T.E., Stewart, D.A., "Enhancement in the thermoelectric figure of merit and breakdown of the Wiedemann-Franz Law in noble metals under strong electron-phonon nonequilibrium," *Journal of Applied Physics* 108, 104907 (2010) – *Selected for the December 2010 issue of the Virtual Journal of Ultrafast Science*.

23. Duda, J.C., Beechem, T.E., Smoyer, J.L., Norris, P.M., Hopkins, P.E., "The role of dispersion on phononic thermal boundary conductance," *Journal of Applied Physics* 108, 073515 (2010).

22. Hopkins, P.E., "Influence of inter- and intraband transitions to electron temperature decay in noble metals after short pulsed laser heating," *Journal of Heat Transfer* 132, 122402 (2010).

21. Beechem, T.E., Duda, J.C., Hopkins, P.E., Norris, P.M., “Contribution of optical phonons to thermal boundary conductance,” *Applied Physics Letters* 97, 061907 (2010).

20. Hopkins, P.E., Phinney, L.M., Serrano, J.R., Beechem, T.E., “Effects of surface roughness and oxide layer on thermal boundary conductance at aluminum/silicon interfaces,” *Physical Review B* 82, 085307 (2010).

19. Hopkins, P.E., Serrano, J.R., Phinney, L.M., Kearney, S.P., Grasser, T.W., Harris, C.T., “Criteria for cross-plane dominated thermal transport in multilayer thin film systems during modulated laser heating,” *Journal of Heat Transfer* 132, 081302 (2010).

18. Duda, J.C., Smoyer, J.L., Norris, P.M., Hopkins, P.E., Beechem, T.E., “Inelastic phonon interactions at solid-graphite interfaces,” *Superlattices and Microstructures* 47, 550 (2010).

17. Duda, J.C., Hopkins, P.E., Smoyer, J.L., Bauer, M.L., English, T.S., Saltonstall, C.B., Norris, P.M., “On the assumption of detailed balance in prediction of diffusive transmission probability during interfacial transport,” *Nanoscale and Microscale Thermophysical Engineering* 14, 21 (2010).

16. Hopkins, P.E., Beechem, T.E., “Effects of propagating and localized modes on the minimum phonon thermal conductivity of layered solids above the plateau,” *Nanoscale and Microscale Thermophysical Engineering* 14, 51 (2010).

15. Hopkins, P.E., Barnat, E.V., Cruz-Campa, J.L., Okandan, M., Nielson, G.N., “Excitation frequency dependence of Auger recombination in surface treated Si wafers,” *Journal of Applied Physics* 107, 053713 (2010).

14. Hopkins, P.E., “Thermoreflectance dependence on Fermi surface electron number density perturbations,” *Applied Physics Letters* 96, 041901 (2010).

13. Hopkins, P.E., “Influence of electron-boundary scattering on thermoreflectance calculations after intra- and interband transitions induced by short-pulsed laser absorption,” *Physical Review B* 81, 035413 (2010) – *Selected for the February 2010 issue of the Virtual Journal of Ultrafast Science*.

12. Hopkins, P.E., Beechem, T.E., Duda, J.C., Smoyer, J.L., Norris, P.M., “Effects of sub-conduction band excitations on thermal conductance at metal-metal interfaces,” *Applied Physics Letters* 96, 011907 (2010).

11. Hopkins, P.E., “Contributions of inter- and intraband excitations to electron heat capacity and electron-phonon coupling in noble metals,” *Journal of Heat Transfer* 132, 014504 (2010).

10. Beechem, T.E., Hopkins, P.E., “Predictions of thermal boundary conductance for systems of disordered solids and interfaces,” *Journal of Applied Physics* 106, 124301 (2009).

9. Hopkins, P.E., Serrano, J.R., “Phonon localization and thermal rectification in asymmetric harmonic chains using a nonequilibrium Green’s function formalism,” *Physical Review B* 80, 201408(R) (2009).

8. Hopkins, P.E., Rakich, P.T., Olsson, R.H., El-kady, I.F., Phinney, L.M., “Origin of reduction in phonon thermal conductivity of microporous solids,” *Applied Physics Letters* 95, 161902 (2009).

7. Hopkins, P.E., Norris, P.M., Tsegaye, M.S., Ghosh, A.W., “Extracting phonon thermal conductance across nanoscale junctions: Nonequilibrium Green’s Function approach compared to semiclassical methods,” *Journal of Applied Physics* 106, 063503 (2009).

6. Hopkins, P.E., Stewart, D.A., “Contribution of *d*-band electrons to ballistic transport and scattering during electron-phonon nonequilibrium in thin Au films using an *ab initio* density of states,” *Journal of Applied Physics* 106, 053512 (2009).

5. Hopkins, P.E., “Multiple phonon processes contributing to inelastic scattering during thermal boundary conductance at solid interfaces,” *Journal of Applied Physics* 106, 013528 (2009).

4. Duda, J.C., Smoyer, J.L., Norris, P.M., Hopkins, P.E., “Extension of the diffuse mismatch model for thermal boundary conductance between isotropic and anisotropic materials,” *Applied Physics Letters* 95, 031912 (2009).

3. Hopkins, P.E., Piekos, E.S., “Lower limit to phonon thermal conductivity of disordered, layered solids,” *Applied Physics Letters* 94, 181901 (2009).

2. Hopkins, P.E., “Effects of electron-boundary scattering on changes in thermoreflectance in thin metal films undergoing intraband transitions,” *Journal of Applied Physics* 105, 093517 (2009).

1. Hopkins, P.E., Kassebaum, J.L., Norris, P.M, “Effects of electron-interface scattering on electron-phonon equilibration in Au films,” *Journal of Applied Physics* 105, 023710 (2009) – *Selected for the February 2009 issue of the Virtual Journal of Ultrafast Science*.

DISTRIBUTION

Quantity	Name of Person	Org. Number	Mail Stop
1	Barnat, E.	1128	1423
1	Beechem, T.	1112	1415
1	Bourdon, C.	1512	0836
1	Brinker, C.J.	1002	1349
1	Chavez, D. - LDRD Office	1911	0359
1	Dimos, D.	1500	0384
1	Duda, J.	1513	0346
1	English, T.	1513	0346
1	El-Kady, I.	1725	1082
1	Gallis, M.	1513	0346
1	Grasser, T.	1512	0826
1	Grillet, A.	1512	0346
1	Harris, C. T.	1132	1314
1	Hattar, K.	1111	1056
1	Ihlefed, J.	1816	1069
1	Jones, R.	8246	9404
1	Kaehr, B.	1815	1349
1	Lash, J.	1510	0825
1	Kearney, S.	1512	0826
1	Medlin, D.	8656	9161
1	Moreno, Y.	1911	0359
1	Peebles, D.	1112	1415
1	Piekos, E.	1513	0346
1	Phinney, L.	1513	0346
1	Rader, D.	1513	0346
1	Ratzel, A.	4800	1469
1	Reinke, C.	1725	1082
1	Serrano, J.	1513	0346
1	Sharma, P.	8656	1413
1	Sullivan, J.	1132	1304
1	Technical Library	9536	0899
1	Torczynski, J.	1513	0346

Sandia National Laboratories